ABSTRACT

Factors affecting the oxidation of magnetite to maghemite and hematite were studied by infrared absorption analysis in conjunction with X-ray diffraction (XRD) and differential thermal analysis (DTA). These factors included particle size and the presence of water vapour.

Infrared absorption peaks were assigned for the three synthetic minerals, and an unsuccessful attempt was made to calculate the activation energies of the magnetite-to-maghemite and the maghemite-to-hematite reactions.

Magnetite appears to oxidize to maghemite via a short-lived "hydroxo" intermediate. Neither the oxidation of magnetite to maghemite nor the crystallographic conversion of maghemite to hematite appear to be simple first- or second-order reactions.

The thesis contains a brief description of the infrared, XRD, and DTA theory, apparatus, and methods, and discusses the information obtained by use of these and ancillary methods.

ACKNOWLEDGEMENTS

The author wishes to express gratitude to his research supervisor, Dr. A.D. Westland, and to Dr. A.H. Gillieson, Group Leader, Spectrochemistry Group, Mineral Sciences Division, Mines Branch, for their continued interest and encouragement throughout the course of this investigation.

Thanks are extended to Mr. R.H. Lake, Technical Officer, Physical Chemistry Group, and to Mr. E.J. Murray and Mr. J.M. Stewart, Technical Officers, Crystal Structure Group, Mineral Sciences Division, for the DTA and XRD studies, respectively. The technical and theoretical contributions of these and many other Divisional personnel are accepted with thanks.

Grateful acknowledgement is extended to the Mines Branch, Department of Energy, Mines and Resources, which provided the time, equipment and financial support for this investigation.

TABLE OF CONTENTS

LIST OF TABLES

LIST OF ILLUSTRATIONS

CHAPTER 1

INTRODUCTION

1.1 Objective of the Study

Magnetite or ferrosoferric oxide, Fe_3O_4, and its metastable oxidation product, maghemite or γ-Fe_2O_3, are crystallographically isomorphous, both having the cubic, inverse-spinel type of crystal structure. Upon heating, γ-Fe_2O_3 undergoes an irreversible transition in structure to hexagonal α-Fe_2O_3, or hematite, thus completing the process of transformation among the three iron oxides.

The characteristic spinel structure has a cation:anion, metal:oxygen ratio 0.75:1.00, whereas the ratio for the γ-oxide is considerably smaller, 0.67:1.00. The generally accepted structure of γ-Fe_2O_3, proposed independently by Hägg[1] and Verwey[2], is thus a defect structure in which the unit cell consists of $Fe_{21.33}\Delta_{2.67}O_{32.00}$, in which the 2.67 cation vacancies Δ are distributed statistically over the 24 possible cation positions. The filling of the cation vacancies by H_2O has been postulated by several workers. Braun[3] has postulated ordering of the γ-Fe_2O_3 spinel structure through the incorporation of water molecules to the limiting hydrogen ferrite spinel of formula $H_4Fe_{20}O_{32}$ (combination), whereas Aharoni *et al.* have suggested combining the accepted oxide $Fe_{21.33}\Delta_{2.67}O_{32}$ with H_2O[4]. The necessity for water in the formation of γ-Fe_2O_3 is shown from the work of David and Welch[5] and of Sinha and Sinha[6], who assumed that hydrogen is incorporated as an anion, i.e., as $(OH)^-$ replacing O^{2-}.

The method of infrared absorption analysis, in conjunction with differential thermal analysis (DTA), and X-ray diffraction (XRD), theoretically appeared to be excellent for determining the exact role of water in the

magnetite-to-hematite transformation and for evaluating the semi-quantitative activation energies of the reacting species. This paper is the result of such an investigation as well as a coincident examination of the effects of variables such as grain size and method of preparation of the starting material, magnetite.

Bagin and Rybak[6a] have made thermal studies of maghemite stabilized by organic impurities, while van Rensburg[6b] has investigated the oxidation of natural magnetite to maghemite and hematite. Correlations between natural and synthetic iron oxide preparations have been made by Schwertmann[6c]. Magnetic and structure properties have been determined by Moessbauer investigations of magnetite by Daniels and Rosencwaig[6d] and of iron oxides including magnetite, maghemite, and hematite by Takada et al.[6e]. Takada et al. were able to observe only one isomer shift in the Moessbauer spectrum of maghemite. The expected isomer shifts due to the octahedral and tetrahedral ferric ions apparently were not resolved.

1.2. Historical Background

Magnetite or lodestone, as it is commonly called, derives its name from Magnesia, a district in Thessaly, where it was originally discovered. Magnets made of magnetite were known in antiquity, possibly before iron itself was put to magnetic use. Natural magnetite is very widespread and large deposits may be found in India, Sweden, South Africa, Russia, Canada, and the United States. Magnetite may be found as both a primary and secondary mineral and may occur in magmatic segregation deposits, in metamorphic deposits, in replacement deposits, in sulfide vein deposits, in stony meteorites, and as an oxidation deposit[6f].

Maghemite was discovered in 1859 by Robbins[7] who was investigating the oxidation of synthetic magnetite. The name "maghemite" was originally

proposed by Wagner[8] in 1927 to refer to such a "magnetic ferric oxide", and early reports of synthetic preparations were by Sosman and Posnjak[9] and Twenhofel[10]. Maghemite is also known as "oxymagnite" or "sosmanite", but will be referred to as maghemite or γ-Fe_2O_3 in this study. In nature, maghemite is a common but not abundant oxidation product of magnetite or dehydration product of lepidocrocite, γ-FeOOH, in iron ores in many parts of the world including Canada. Canadian occurrences have been studied extensively by McLeod[10a] and include those of Baffin Island, Labrador, and Steep Rock iron mines. Maghemite rarely occurs as discrete, homogeneous grains amenable to separation for conventional analysis or application. It does form as a fine, usually irregular thread-like product in and around magnetite grains under oxidizing conditions, and with exceptionally favourable circumstances, it may completely replace magnetite crystals.

Commercial applications of maghemite relate to its inertness to corrosion and to its electrical and magnetic properties which will be mentioned in a subsequent section.

1.3. Commercial Applications of Ferrosoferric and Ferric Oxides

Iron, calculated as oxides, composes 7%, by weight, of the earth's crust. Because of their wide distribution, the iron oxides were not only an important ore but they probably became the first coloring materials. In fact, as a group, they enjoy the longest fading and permanency tests on record. They are unaffected chemically or physically by sunlight, moisture, salts, weak acids or alkalies. As pigment components they are non-bleeding, permanent in color, opaque to ultraviolet light, and have excellent covering power and produce hard impervious films. A review of the applications of the iron oxides in the pigment industry may be found in a paper by Love and Ayers[11].

Magnetite and maghemite have found widespread application as high-frequency semiconductors in microwave devices because of their high resistivities, 10^6 to 10^7 ohm-cm., which minimize eddy current losses in high-frequency magnetic fields. Eddy currents arise because a temporary change of magnetic induction flux penetrating a conductor causes a flow of electric current in the opposite direction, resulting in energy loss by Joule heating. The two oxides are widely used in coils, transformers, and switches in radio, television, and telecommunications engineering, in aerial rods, in accelerators for elementary particles, and in digital computers. Maghemite is extensively used as the magnetic material in recording media.

Technically useful magnetite, maghemite, and hematite are generally prepared by a sintering process. The quantities that can be varied during sintering, such as firing temperature, atmosphere, and condition of materials before firing, will determine the sensitivity of the products to inhomogeneity and partial reduction or oxidation.

CHAPTER 2

THEORETICAL ASPECTS OF THE STUDY

2.1. Outline of Theoretical Considerations

As stated in the Introduction, most of the experimental work for this thesis was accomplished by the use of three basic instrumental techniques: DTA, XRD, and infrared absorption. For this reason, a short theoretical summary of each method will be given in the following sections. For the most part, the methods will be explained in the order of their application to the study.

2.2. Differential Thermal Analysis (DTA)

DTA consists of simultaneously heating a test sample in conjunction with a reference sample of inert material which does not undergo any reaction in the relevant temperature range. Fundamentally, the difference in electric signal strength passed by the test and reference samples during the heating process is recorded graphically via thermocouple connections to the two samples. The resultant graph records temperature (or time, since a constant heating rate is employed) on the abscissa and differential electromotive force on the ordinate scale.

The degree of reaction within the analytical sample is recorded as an exothermic "peak" or an endothermic "valley" at the reaction temperature. Since exotherms generally predominate in DT work, both exotherms and endotherms will be referred to as "peaks". An exotherm results from heat production within the test sample due possibly to recrystallization processes or to oxidation, while an endotherm results from absorption of energy as would occur during dehydration processes. In other words, exotherms result from

the release of thermal energy and subsequent stabilization of the sample system, while endotherms arise from the absorption of thermal energy and the subsequent instability of the system.

In general, the amount of reaction occurring for a given sample weight at a given temperature may be measured by the area under the peak at that temperature. The area depends on such properties as the thermal conductivity, bulk density, specific heat, and thermal diffusivity of the sample. These properties are specific to individual materials and in many cases may be considered constant over the relevant temperature ranges of analysis. However, other properties, such as grain size and moisture content of the analytical material, are specific to the preparative method and may cause variations in the peak areas and/or shifts in temperature of the peaks. The peak areas are independent of the heating rate, but the peak temperatures are not.

Because the principal function of the DT analyses in this investigation was to provide a convenient means of treating magnetite under controlled conditions of atmosphere, temperature and time, no attempt will be made to derive mathematical expressions to account for the properties of the preceding paragraph in relation to the sample peak areas. Instead, the analyses will serve as reaction-sequence checks against similar DT investigations of magnetite achieved by other workers.

It should again be emphasized that DT reactions are dynamic processes, involving the absorption or emission of thermal energy, rather than equilibrium or static processes.

2.3. X-Ray Diffraction (XRD) Analysis

2.3.1. Crystal Structure Considerations in XRD

A perfect crystal consists of the repetition of a single very small unit of structure called the unit cell in a regular way so as to fill the volume occupied by the crystal. Such a unit cell may be described in terms

of a set of three crystal axes a, b, and c which may or may not be mutually perpendicular, depending on the crystal system so defined. Along each axis, an atom will repeat at a distance called a, b, and c, respectively. These distances are called the unit translations along the respective axes.

The arrays of atoms which constitute crystal faces are described in terms of their intercepts with the a, b, and c axes. The Miller indices so derived are small common integral multiples of the reciprocals of the a, b, and c intercepts. These are designated h, k, and ℓ, respectively, and may be positive, negative, or zero.

The crystal axes are conventionally chosen to yield a coordinate system of the highest possible symmetry as described by the axial lengths a, b, and c and the interaxial angles α, β, and γ between b and c, a and c, and a and b, respectively. The positioning of the X-ray reflections from a crystal depends on the shape, size, and type of its unit cell or lattice, while the relative intensity of these reflections depends on the arrangement or symmetry and the type and number of the atoms within the cell.

2.3.2. Conditions for X-ray Diffraction by Crystals

If one considers the high-density atomic arrays within a crystal to consist of an infinite number of equally spaced parallel hkℓ planes, then the necessary condition for scattering-in-phase by these planes is that the path difference of the X-ray beams striking adjacent planes must differ by an integral number of wavelengths. Such a situation can be seen by reference to Figure 2.3.2., where:

$$\Delta = 2\overline{AB} = 2\, d_{hk\ell} \sin\theta$$

If both the planes are to scatter in phase, the path difference Δ must equal an integral number of wavelengths, and:

$$n\lambda = \Delta = 2d_{hk\ell}\sin\theta \qquad 2.3.2$$

where: n = integer

λ = X-ray wavelength in Ångstroms (Å)

$d_{hk\ell}$ = interplanar spacing in Å determined by the Miller indices $hk\ell$

θ = glancing angle, or complement of the angle of incidence i, in degrees or radians.

This condition for in-phase scattering is known as Bragg's Law, and the scattered X-rays are said to constitute a reflection which is designated $hk\ell$, written without parentheses.

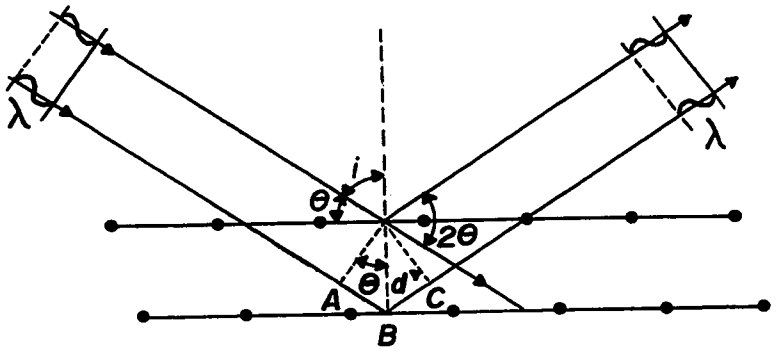

FIGURE 2.3.2 - Conditions for Reflection from Scattering Centers Confined to Two Parallel Planes

2.3.3. The Unit Cells of Magnetite, Maghemite, and Hematite

The cubic unit cell of the spinel structure, to which magnetite and maghemite belong, is shown in Figure 2.3.3.[12]. For magnetite, of space group $O_h^{7(12a)}$, the cell contains thirty-two oxygen, sixteen trivalent iron and eight divalent iron atoms, or a total of eight "molecular" units. The cell consists of two groups of four cubes, or octants. The ionic positions are different in any two octants sharing a face and a corner and they are the same in two octants sharing an edge. Each octant contains four oxygen ions, denoted by large spheres in Figure 2.3.3, on the body diagonal of the octant and lying at the corners of a tetrahedron. The left-hand octant contains, in the centre, an iron ion denoted by a small unshaded sphere, surrounded by a tetrahedron of oxygen ions. This iron is therefore designated a tetrahedral- or A-ion. The right-hand octant shows four iron ions, represented by small shaded spheres, each surrounded by six oxygen ions. Such metal ions are termed octahedral- or B-ions.

The oxygen sublattice contains sixty-four A-interstices, eight of which are occupied by iron ions, and thirty-two B-interstices, sixteen of which are occupied by iron ions. In the inverse spinel structure to which magnetite and maghemite belong, divalent Fe^{2+} ions occupy eight, or one-half, of the occupied B-interstices, while trivalent Fe^{3+} occupy both A- and B-interstices, eight in each of the two positions.

As stated in the Introduction, the unit cell of maghemite is a defect structure consisting of $Fe_{21.33}\Delta_{2.67}O_{32.00}$, where the cation vacancies Δ are distributed statistically over the twenty-four possible cation positions. The occurrence of such a vacancy structure has been the object of several investigations in recent years with regard to the location of

FIGURE 2.3.3

UNIT CELL OF THE SPINEL STRUCTURE OF MAGNETITE

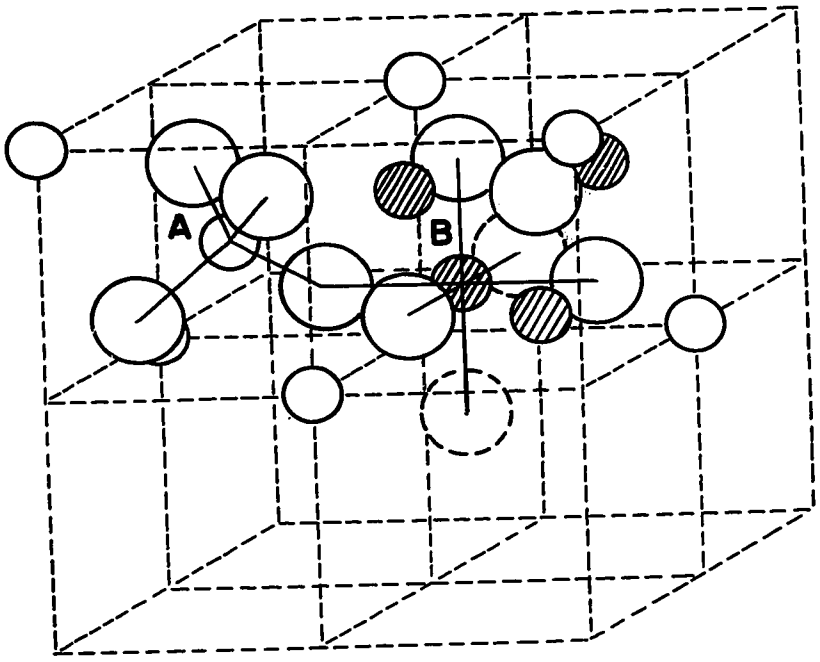

A- tetrahedral site display, upper octant

B- octahedral site display, upper octant

- oxygen ion

- oxygen ion in lower octant

- tetrahedral iron ion

- octahedral iron ion

the vacancies in either the octahedral or tetrahedral sites of the cation sublattice[13,14,15]; Hasegawa et al.[14] and Ferguson and Hass[15] have conclusively established, by X-ray and neutron diffraction studies, respectively, the existence of ordered vacancies on octahedral interstices only. Such ordering of vacancies at octahedral interstices has been confirmed by the Moessbauer studies of Daniels and Rosencwaig[6d].

Such ordered vacancies result in the appearance of extra diffraction lines which do not correspond to lines in the pattern for magnetite. These extra reflections have led to the generally accepted postulation of a tetragonal unit cell for maghemite, consisting of an identical oxygen network to that of magnetite, but with a vacancy at one cation site out of nine. This results in an average of 2 2/3 vacancies for the maghemite unit cell. van Oosterhout and Rooijmans[15a] have found ordered vacancies and postulated a tetragonal supercell of space group $P4_1$ or $P4_3$ with 32 "molecules" Fe_2O_3 and c/a=3. The assumption of such a tetragonal cell implies a reduction of symmetry from that of the spinel structure, the appearance of extra XRD lines, and the variation of intensity of those lines associated with the ideal spinel cubic unit cell. These differences will be outlined more fully in the Results and Discussion.

Pauling and Hendricks[16] first determined the hexagonal crystal structure of hematite and this structure was later refined by Blake et al.[17] with respect to minor shifts in atomic coordinates. Blake et al. assigned the hematite structure to space group $R\bar{3}c$. The XRD pattern of the hexagonal hematite studied in this investigation will again be dealt with in the Results and Discussion.

2.4. Infrared Absorption Analysis

2.4.1 Basic Absorption Theory

If one considers a vibrating heteropolar atomic species A-B, then the vibration of such a species will result in variation of the

interatomic distance between A and B with consequent variation in the dipole moment. If the species were homopolar, there would be no variation in the dipole moment and no infrared absorption would occur. Often polyatomic molecules having elements of symmetry will not produce infrared absorptions because no change in dipole moment will occur throughout a vibration.

In summary, an oscillating dipole will absorb infrared radiation whose frequency is equal to its vibration frequency and will transmit unchanged all other frequencies. In quantum mechanical terms, if the alternating dipole is to absorb the energy of a light quantum, the energy of the quantum must be exactly equal to the energy difference between two of the allowed energy levels of the oscillator. Such a situation results in the absorption spectrum of the species, and the frequency range over which such absorption will occur is generally referred to as an absorption band or absorption peak with finite width.

Considering again the heteropolar species A-B, this system, to a first approximation, will obey Hooke's Law of harmonic motion and vibrate with a frequency given by:

$$\nu = \frac{1}{2\pi c}\sqrt{\frac{k}{m_r}} \qquad 2.4.1$$

where: c = velocity of light,

k = force constant,

m_r = reduced mass $= \dfrac{m_A m_B}{m_A + m_B}$.

The force constant k is a complex function of the bond distance between A and B. In general, the larger the bond length, the weaker the bond and the smaller the force constant and frequency. Such factors as the degree of covalency of the bond and the degree of interatomic interaction between nearest-neighbour atoms and A or B tend to alter the magnitude of the force constant.

2.4.2. Types of Infrared Absorption

When dealing with harmonic oscillators, one is concerned with only a single type of vibrational transition; that is, between the ground vibrational energy state and the first excited energy state. This transition is known as the fundamental absorption or simply the fundamental.

However, the vibrations of real molecules are not strictly harmonic, and the anharmonicity results in the occurrence of overtone and/or combination absorptions. Such absorptions are generally at least an order of magnitude less intense than fundamentals and will not be considered further in the present study.

2.4.3. The Number of Expected Fundamentals

For a molecule of N atoms, each atom has three degrees of space freedom corresponding to the three Cartesian coordinates, resulting in a total of 3N degrees of freedom for the entire molecule. However, three of these degrees describe translation along the space-fixed Cartesian coordinates, and a further three describe rotation of the molecule as a whole about its three mutually perpendicular axes through the center of mass. Therefore, the number of fundamental vibrations of a general N-atom

nonlinear molecule is just 3N-6.

In the present investigation concerning the mineral species magnetite, maghemite and hematite, the minerals do not behave as individual ionic molecules, but as lattice arrays influenced by relatively strong lattice energies. The arrays contain eight molecules per unit cell and may in fact be composed of entire single crystals atomically arranged with various symmetry properties. The number of observed infrared absorption fundamentals will therefore depend on the size of the lattice unit one must consider and the symmetry operations relating to this unit. These factors are functions of the degree of covalency of the individual vibrating species, the total lattice energy of the unit, and the degree of inter- and intra-atomic interaction within and between the lattice arrays. For these reasons, no attempt will be made to determine the number of expected fundamentals.

2.4.4. The Intensity of Observed Absorption Peaks

The absorption of infrared radiation by matter may be mathematically expressed by the Beer-Lambert-Bouguer Law which states:

$$A = -\ell n\left(\frac{I}{I_o}\right) = b\sum_{n=1}^{N} a_n c_n, \qquad 2.4.4.$$

where A = intensity of absorbance or absorption strength,

I_o = incident intensity,

I = transmitted intensity,

a = absorptivity,

b = path length,

c = concentration, and

N = component number of the system.

If one can assume for a reacting system that the reactants have absorption frequencies that are completely distinct from those of the products, then the course of the reaction may be followed by carefully recording the decrease in intensity or peak height of the fundamental absorption for one particular reactant. The rate of disappearance of that reactant can be determined by following the changes in peak height as a function of time.

2.4.5. Estimation of Activation Energies

The activation energy is the minimum energy that a molecule must acquire before undergoing a reaction. The activation energies for the maghemite-to-hematite and magnetite-to-maghemite reactions, ideally first- and second-order in terms of mineral concentrations, may be calculated from the following equations. In this study, conditions were chosen such that temperature varied linearly with time.

(a) First-Order Reaction

A first-order reaction is one in which the reaction rate is directly proportional to the concentration of the reacting species. In the present investigation, such a reaction could be the conversion of maghemite to hematite:

$$\gamma\text{-}Fe_2O_3 = \alpha\text{-}Fe_2O_3$$

For such a reaction at a given time t,

$$k = \frac{-1}{c}\frac{dc}{dt} \qquad 2.4.5(a)$$

where k = rate constant

c = concentration of reactant

t = time

However, the rate constant k may be related to the absolute temperature T of the reaction by the Arrhenius Equation:

$$k = Pe^{-E_a/RT} \qquad 2.4.5(b)$$

For the present study, the temperature T is directly proportional to the reaction time t, so that

dt = XdT, where X = constant.

Combining 2.4.5(a) and 2.4.5(b) with respect to T,

$$\ell n\ c_1 - \ell n\ c_2 = \ell n\left(\frac{c_1}{c_2}\right) = P' \int_{T_1}^{T_2} e^{-E_a/RT}\, dT \qquad 2.4.5(c)$$

where P, P' = constants,

E_a = activation energy, first-order reaction, in cal/mole,

R = gas constant = 1.99 cal/mole deg,

c_2, c_1 = concentrations of reactants at temperatures T_2, T_1, respectively, and

T = absolute temperature in degrees K.

(b) Second-Order Reactions

If the reaction rate is proportional to the concentration of two reactants, the reaction is of second order. Such a reaction could be:

$$2Fe_3O_4 + \tfrac{1}{2}O_2 = 3Fe_2O_3 \quad (\gamma\text{- and/or } \alpha\text{-})$$

provided that the oxygen is maintained in excess as it is assumed in the present study.

For such a reaction,

$$k = -\frac{dc}{c^2 dt} \qquad 2.4.5(d)$$

and, as before, dt = XdT, where X = constant. Again employing the Arrhenius Equation, and integrating the right-hand side of the equation with respect to T:

$$-\int_{c_1}^{c_2} \frac{dc}{c^2} = Q \int_{T_1}^{T_2} e^{-E_a/RT}\, dT,$$

where Q = constant,

E_a = activation energy, second-order reaction, in cal/mole

or,

$$\frac{1}{c_1} - \frac{1}{c_2} = Q \int_{T_1}^{T_2} e^{-E_a/RT}\, dT \qquad 2.4.5(e)$$

If one assumes the direct proportionality of the fundamental infrared absorption peak heights or intensities to the initial and final concentrations c_1 and c_2, respectively, then these variables may be incorporated in the activation energy equations just developed.

2.4.6. Infrared Determination of Water

Water in crystalline species may be classified as either lattice water or co-ordinated water, with no definite borderline between the two. Lattice water refers to water molecules trapped in the crystal interstices and held by weak hydrogen bonds to the anion or the metal, while co-ordinated water refers to water molecules partially covalent-bonded to the metal.

Lattice water absorbs in the infrared region between 3600 and 3200 cm^{-1}, due to OH stretching vibrations, 1630 to 1600 cm^{-1}, due to HOH

bending, and possibly somewhat below 600 cm^{-1} due to librational modes resulting from rotational oscillations of the water molecules and restricted by interactions with neighbouring atoms.

In addition to the three fundamental modes of lattice water, three additional modes will become infrared active if the metal-oxygen bond is sufficiently covalent. These are the rocking or in-plane bending vibration, the wagging or out-of-plane bending vibration, and the metal-oxygen stretching vibration of the cation and the oxygen of the water. In general, such absorptions should all appear below 1000 cm^{-1} and the relative intensities of the stretching and bending vibrations may vary to a great extent depending on the nature of the covalent bond. The greater the covalency, the larger the stretching intensity compared to the bending intensity.

The possibility of forming hydroxo, (OH), complexes must also be considered in the present study. The hydroxo group can readily be distinguished from the co-ordinated water group because, although each exhibits the OH stretch between 3600 and 3200 cm^{-1}, the hydroxo complex lacks the HOH bending mode below 1600 cm^{-1}, and can in fact produce a vibration below 700 to 800 cm^{-1} due to hydroxyl bridging. Such bridging has been investigated by Ferraro *et al*.[18] in chromium (III) and iron (III) complexes.

2.5. Oxidation Reactions Specific to This Study

The oxidation of Fe_3O_4 to γ-Fe_2O_3 and thence to α-Fe_2O_3 involves two distinct reaction processes[19];

(a) $Fe_3O_4 \rightarrow \gamma$-$Fe_2O_3$: This is a topotactic process in which accord between the initial and resultant lattices in three dimensions occurs. Both magnetite and maghemite have the cubic close-packed oxygen sublattices with the inverse

spinel structure.

(b) γ-$Fe_2O_3 \rightarrow \alpha$-$Fe_2O_3$: This is an epitaxial process in which accord between the initial and resultant lattices occurs in two dimensions. α-Fe_2O_3 has a hexagonal close-packed oxygen sublattice with ferric ions filling 2/3 of the octahedral positions between successive oxygen layers. The ordering of layers shifts from abcabc in maghemite to abab in hematite.

Feitknecht[20] has extensively investigated the oxidation processes in magnetite. He found that Fe_3O_4 particles with specific surface areas less than 4 m^2/g (approx.), oxidize by a "nucleation mechanism", in which a concentration gradient of iron ions occurs in an outward direction. Nuclei of α-Fe_2O_3 are formed in a mixed phase which decomposes into α-Fe_2O_3 and Fe_3O_4. The remaining Fe_3O_4 is oxidized directly to α-Fe_2O_3, and the rate-controlling step is the diffusion of iron ions through the oxygen sublattice. The last remnants of Fe_3O_4 are oxidized only at temperatures exceeding 400°C.

However, Fe_3O_4 with a specific surface greater than 4 m^2/g was found to react quite differently. In this case, the oxidation occurs as a continuous, one-phase reaction for which the following mechanism has been proposed: the oxygen molecules absorbed on the surface of the Fe_3O_4 particles are converted to O^{2-} ions by take-up of electrons in the conversion of ferrous to ferric ions; the O^{2-} ions attach themselves to the outside of the lattice, and this is presumably the rate determining process; the cation vacancies between the O^{2-} ions are filled by an immediate and even redistribution of iron ions within the lattice. Such an oxidation process takes place between 150 and 400°C and produces maghemite.

The γ- $\rightarrow \alpha$-Fe_2O_3 conversion occurs as does the $Fe_3O_4 \rightarrow \alpha$-$Fe_2O_3$

transformation; that is, it is epitaxial in nature, involving only the shifting of oxygen layers from the abcabc ordering of the cubic close-packed maghemite oxygen layers to the abab ordering of hexagonally close-packed hematite oxygen layers.

In summary, the reaction mechanism by which Fe_3O_4 is oxidized is strongly determined by particle size and appears to be influenced to a great extent by factors such as water and impurity content and crystal perfection. Water appears to play a part in transferring the iron ions to new lattice sites, and the presence of internal strain and its partial relief by dislocations appears essential to the initiation of topotactic changes which proceed through the transformation of domains.

CHAPTER 3

THE EXPERIMENTAL PROCEDURES

3.1. Preparation of Magnetite

Extensive investigations of the preparation and properties of magnetite in relation to its oxidation products have been made by Feitknecht and Lehmann[21] and by Hasegawa *et al.*[14].

Four basic methods of synthesis have been attempted by various workers:

(i) Precipitation from a ferrous-ferric salt solution. This synthetic procedure was initially attempted by LeFort[22], who precipitated with concentrated ammonia a solution of 0.2 molar ferric chloride, ($FeCl_3$), and 0.1 molar ferrous sulphate, ($FeSO_4$).

(ii) Oxidation of ferrous hydroxide, ($Fe(OH)_2$). This method as used by Eichenberger[23] involved the slow oxidation of ferrous hydroxide in dilute sodium hydroxide, (NaOH), by passing through the solution 0.5% oxygen in nitrogen.

(iii) Reduction of goethite, (α-$Fe_2O_3.H_2O$), or hematite, (α-Fe_2O_3). The reduction may be achieved by passing hydrogen saturated with water vapour over the material at a temperature exceeding 400°C.

(iv) Oxidation of vapour-coated iron. Iron may be vapour-coated under vacuum in a very thin high-purity layer and oxidized to magnetite by exposure to air.

Of the foregoing methods of preparation of magnetite, the products of procedures (i) and (ii) were found to be likely to contain a few per cent water even after drying. Procedures (iii) and (iv) were found to produce

larger grains of magnetite by approximately an order of magnitude, while method (iv) was the only procedure likely to produce completely anhydrous magnetite. Methods (i), (ii), and (iv) tend to produce nearly stoichiometric magnetite with respect to ferrous iron content, while Method (iii) produces magnetite with excess ferric iron.

In the present study, attempts were made to synthesize magnetite by procedures similar to those of Methods (i) to (iii) and to correlate the properties of the respective products with the preparative procedures. A description of each method is given in the following sections.

(a) High-Temperature Reduction of Hematite

Reagent-grade Baker and Adamson α-ferric oxide of 99.00% minimum purity was pelletized at 20,000 lb/in^2. Principle impurities were: Si 0.10%, Mn 0.06%, Al 0.05%, Mg 0.04%, Ni 0.04%, and Cu and Ti 0.01%, as determined by semi-quantitative spectrochemical analysis. The pellets, in zirconium oxide furnace boats, were placed at the centre of a horizontal electric tube furnace. During warm-up, argon was passed through the furnace tube over the pellets until a temperature of 1100°C was reached. The temperature was maintained at 1100°C for 18 hours, during which time a reducing gas consisting of a 9:1 volume ratio of CO_2:H_2 was passed through the furnace at approximately 300 cc/min. The furnace was turned off and the reduced hematite was immediately vacuum-desiccated over anhydrous magnesium perchlorate ($Mg(ClO_4)_2$) in order to retard decomposition and/or oxidation during cooling.

The reactions occurring during the reduction process at 1100°C were:

$$H_2 + CO_2 = CO + H_2O \quad (1)$$

$$CO + 3Fe_2O_3 = 2Fe_3O_4 + CO_2 \quad (2)$$

The magnetite was oxidized in both anhydrous and water-vapour saturated air by the differential thermal method to temperatures of 350, 415, 650, 1050, 1120, and 1200°C, and the oxidation products were analyzed by X-ray diffraction (XRD). The surface areas of the magnetite and the starting material, hematite, were measured by the Brunauer-Emmett-Teller (BET) N_2 absorption method.

The reduction parameters and the surface area of the resultant magnetite are summarized in Table 4.1, and the DT curves to 1000°C are shown in Figure 4.2.1.

(b) Precipitation By Oxidation Of Ammoniacal Ferrous Chloride Solution

"Baker-Analyzed" hydrated ferrous chloride, ($FeCl_2.4H_2O$), was dissolved in distilled water and the pH's of the different solutions were brought to 8.5, 11.0, and 12.8 in successive experiments by adding NH_4OH to the sealed reaction flasks. After reaching the desired pH, air was bubbled through a gas dispersion tube into the solution which was agitated by magnetic stirring. For successive runs, the air flow was varied from 1 to 150 ml/min and the flow time from 0.5 to 5.0 hr in 0.5-hr increments. After completion of the reaction, the solvent was decanted, the precipitate was washed thoroughly in air-free 1:1 acetone:water solution and filtered to a paste. The precipitate was then dried under vacuum over $Mg(ClO_4)_2$. The entire preparation and separation procedure was performed in a nitrogen atmosphere to avoid extraneous oxidation reactions.

The reactions were:

$$2NH_4OH + FeCl_2 = 2NH_4Cl + Fe(OH)_2 \quad (3)$$

$$3Fe(OH)_2 + \tfrac{1}{2}O_2 = Fe_3O_4 + 3H_2O \quad (4)$$

The specific surface of the precipitate was derived from the BET method and is given in Table 4.1 along with a summary of the reaction conditions used.

(c) Reduction of a Magnetite-Goethite Mixture

A sample batch of synthetic precipitated magnetite called "Mapico Black", of quoted 99.0% minimum purity, was obtained from the Columbian Carbon Company, New York, N.Y. Subsequent semi-quantitative spectrochemical analysis revealed the following impurities: Mg 0.1%, Mn 0.09%, Ti 0.007%, and Co 0.02%. However, a determination of ferrous iron, Fe^{2+}, showed only 16.2% Fe^{2+}, whereas stoichiometric Fe_3O_4 or ($FeO.Fe_2O_3$) should contain 24.1% Fe^{2+}. A preliminary XRD analysis of Mapico Black indicated goethite, (α-$Fe_2O_3.H_2O$) as a minor impurity. It was therefore decided to reduce the Mapico Black and bring its Fe^{2+} content to the stoichiometric level.

Five samples of Mapico Black were reduced at moderate temperatures in a $CO:CO_2$ atmosphere. The reducing-gas flow was maintained throughout an 18-hr cooling period. The reduced samples (RMB) and their conditions of reduction are listed in Table 4.1. Ferrous iron determinations were made by titration with ceric ammonium nitrate according to Donaldson[24], whereas total iron (ferrous and ferric) was found by a modified Zimmermann-Reinhardt process, titrating with potassium dichromate ($K_2Cr_2O_7$). Surface determinations were made on the Mapico Black and of RMB 1, 2, 4, and 5 by use of a Perkin-Elmer Sorptometer 212-D and the Brunauer-Emmett-Teller method. The surface areas are also presented in Table 4.1.

After the reduction reactions and the cooling of the oven, the samples were then vacuum-desiccated over $Mg(ClO_4)_2$, and RMB #5 was chosen, from the surface area and XRD measurements, as the best product for further

experimentation.

Prior to further experimentation, RMB #5, which had been prepared in two 15-g batches, was dried for 24 hr in a vacuum oven between 105 and 110°C. The portion not immediately used was stored under vacuum over $Mg(ClO_4)_2$ to prevent the adsorption of atmospheric water and the oxidation of the material.

3.2.1. The DTA Apparatus

The furnace employed was of the horizontal-tube type in which the resistance wire was Kanthal cylindrically-shaped and clamped in a saddle about the sample-tube port. The furnace insulation was magnesium oxide powder. The furnace temperature was controlled by a Boston "Ratiotrol" variable-speed motor and a 230-volt Variac auto-transformer with a 20-ampere rating. Such a furnace assembly is shown in Figure 3.2.1(a).

The temperature-measuring and difference thermocouples, of platinum versus platinum/13% rhodium-alloy, were used because of their stability and inertness over a high temperature range. The recording equipment consisted of a Leeds and Northrup stabilized DC microvolt amplifier and a 2-pen, 10-inch strip-chart recorder which was linearly calibrated for the Pt vs. Pt/13% Rh thermocouple. One pen recorded the ambient temperature while the other recorded the differential thermal curve. The recorder had a millivolt-measuring function with a -1 to +1 millivolt range continuously expandable to ±10 millivolts; the sensitivity range was 5 microvolts to 2000 microvolts per half-scale deflection.

A mullite tube was employed to carry the sample-holder and the thermocouple assembly in the furnace port. The palladium sample-holder contained two identical wells for the sample and reference materials. The

junctions of the difference thermocouple were fitted in the centres of the two wells via holes drilled through the walls of each cavity. The ambient-temperature-measuring thermocouple was fitted in a third hole in the sample holder located between the two wells. This arrangement resulted in an equal heating effect on the three thermocouple junctions when the furnace was in operation. The sample-tube and holder assembly are shown in Figure 3.2.1(b) and 3.2.1(c), respectively.

3.2.2. DTA of Magnetite Preparations

Since similar sample sizes and techniques were used for the DTA of the reaction products of the high-temperature reduction of hematite and the RMB #5, the following description of the procedure applied to both products. Only the DTA temperature maxima varied between the treatments.

DTA were carried out on the reduced hematite and RMB #5 under constant conditions. Samples, weighing between 0.6 and 0.7 g, were analyzed in flowing argon, in wet air produced by bubbling air through an 80°C water bath, and in dry air produced by passing air through calcium chloride ($CaCl_2$) and copper sulphate ($CuSO_4$) prior to passage over the sample. The argon was dried in a like manner before admission to the sample chamber.

In each analysis, a palladium sample holder was employed with α-alumina (α-Al_2O_3) as the reference standard. The reference material was chosen because of its availability and stability over the temperature range of interest. A temperature increase of 3°C/min was maintained throughout the analyses, as measured by a platinum-rhodium thermocouple, around whose junction the sample was lightly tamped. The gas-flow rate was kept as constant as possible, approximately 0.5 ℓ/min, between individual analyses.

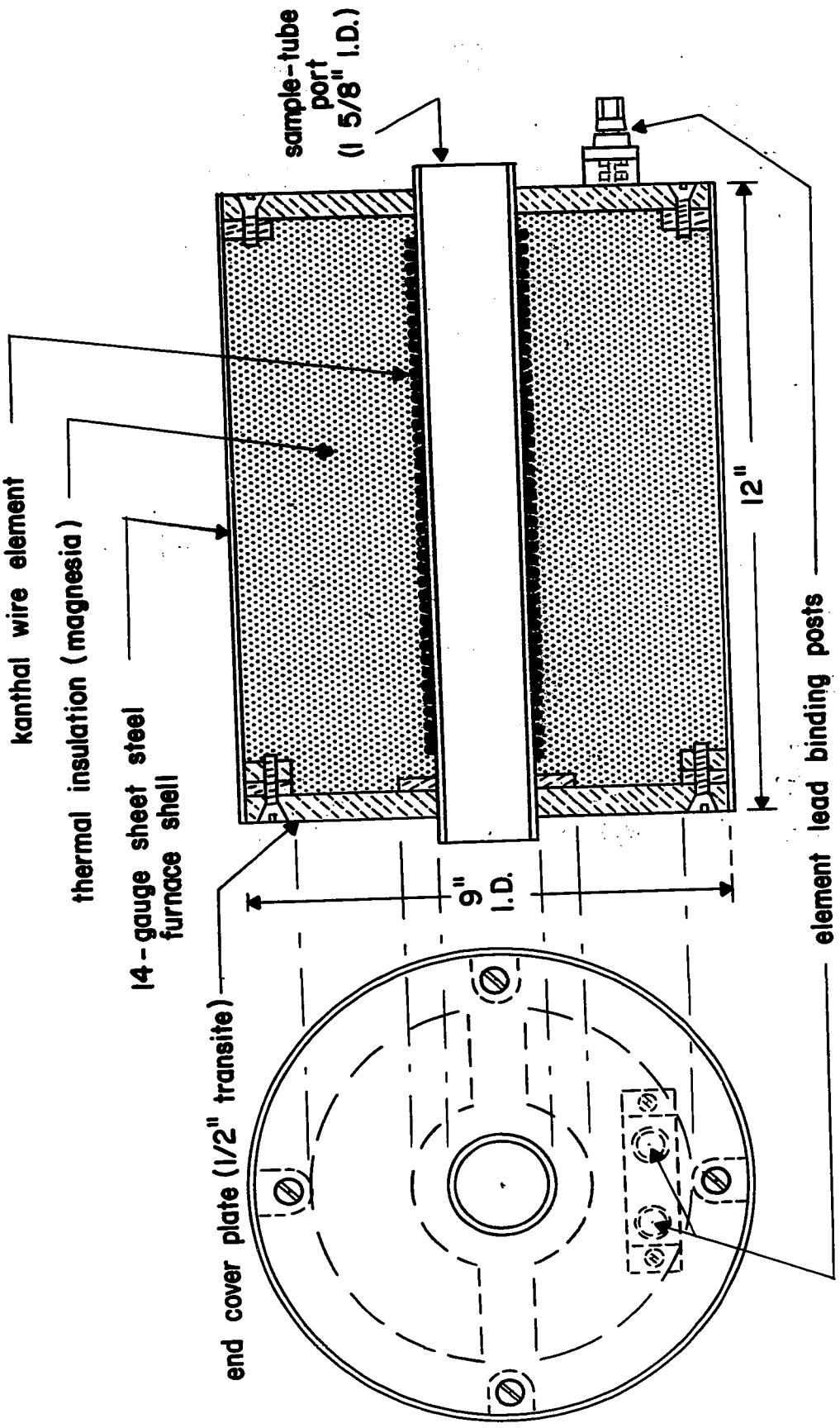

FIGURE 3.2.1(a) KANTHAL-ELEMENT FURNACE

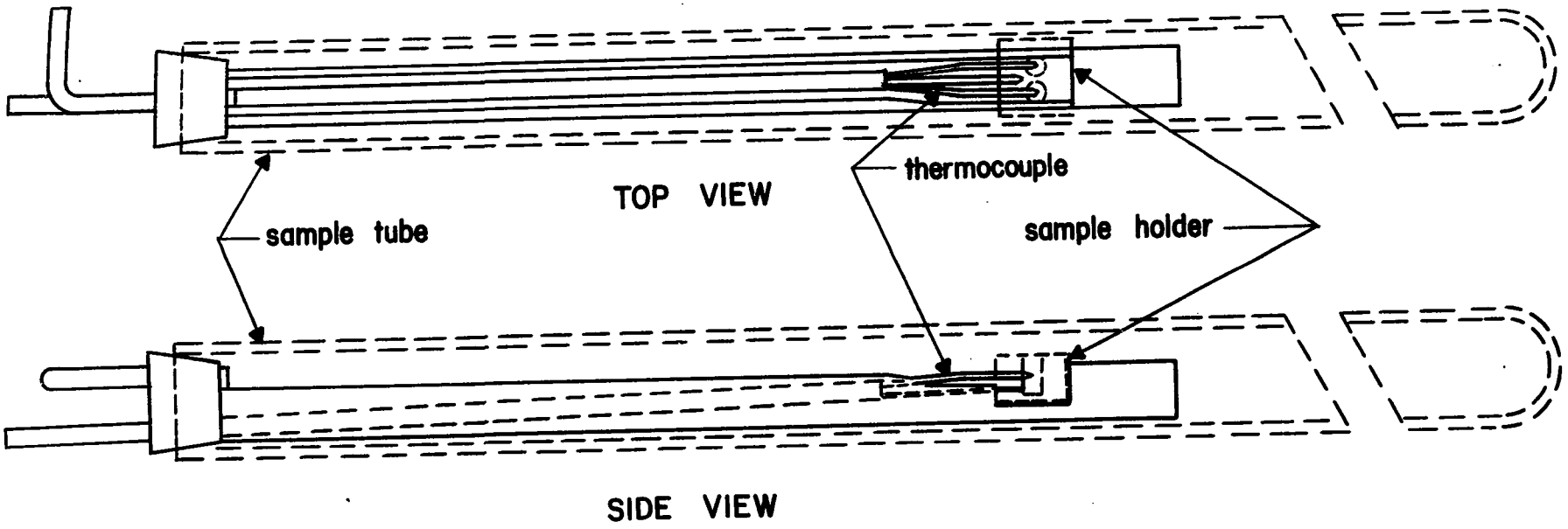

FIGURE 3.2.1(b) MULLITE SAMPLE-TUBE ASSEMBLY CONTAINING SAMPLE HOLDER AND THERMOCOUPLE

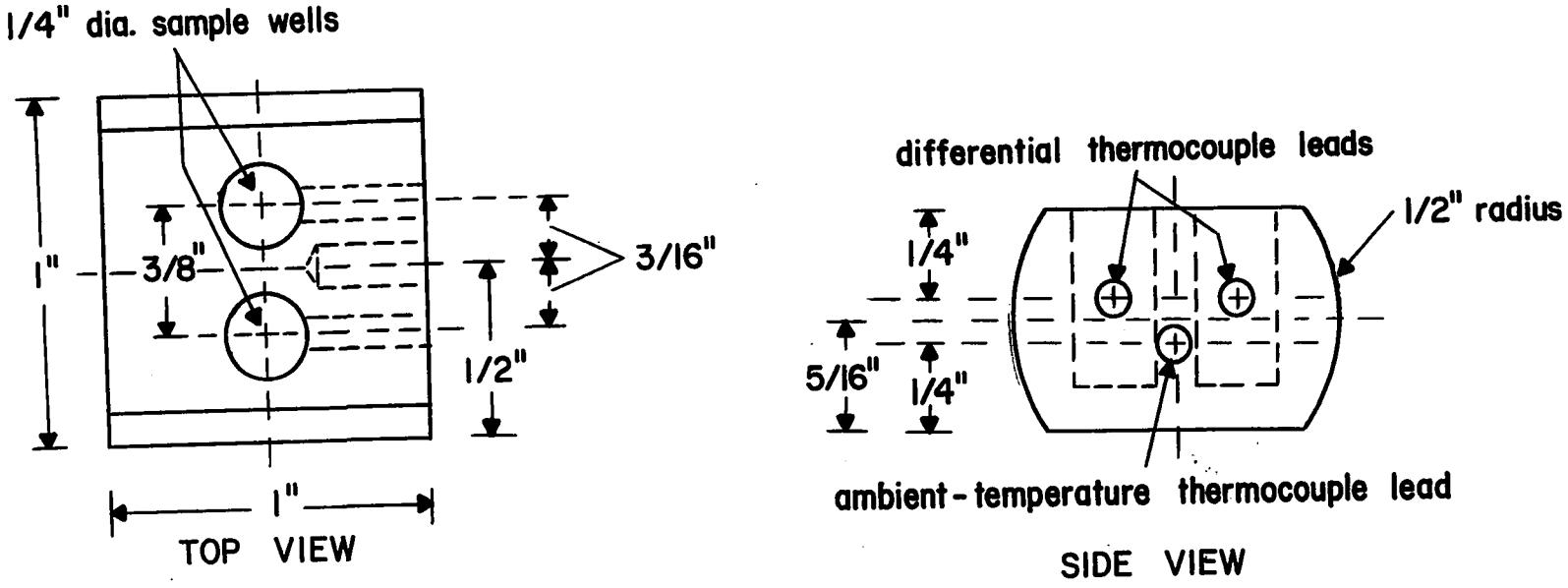

FIGURE 3.2.1(c) SAMPLE HOLDER ARRANGEMENT

Following the preliminary DTA, smaller samples, weighing between 0.2 and 0.25 g were again subjected to DTA under the above conditions but at different furnace shut-off temperatures. The reduced hematite was taken to maximum temperatures of 350, 415, 650, 1050, 1120, and 1200°C in individual tests in both wet and anhydrous atmospheres, while RMB #5 underwent wet oxidation at temperatures between 275 and 650°C and dry oxidation between 234 and 760°C. Upon reaching the desired temperature maxima, the DTA furnace was shut off and the samples were air-quenched to room temperature.

The DT curves for reduced hematite and RMB #5 are illustrated in Figures 4.2.1 and 4.2.2, respectively.

To test for the possible presence of water in RMB #5 even after its formation by the reduction of MB at 400°C, a thermogravimetric analysis (TGA) was made on 2.25 g of RMB #5 to 800°C in a flowing helium atmosphere. A Stanton Recording Thermobalance was employed at a heating rate of 6°C/min. The resulting curve is shown in Figure 4.2.3.

3.3.1. The Debye-Scherrer XRD Powder Method

Several experimental techniques have been developed for realizing XRD conditions, the most powerful of which depends on the study of a single crystal. However, because of the apparent particle-size dependence of the magnetite-to-maghemite reaction, a single-crystal study was impossible in the present investigation. Instead, the Debye-Scherrer method, which utilizes crystal particles a few microns in size, was employed.

The specimen for diffraction filled a thin-walled glass capillary tube of 0.2 mm diameter and cameras of 57.3 mm and 114.6 mm diameter were used to record the X-ray diffraction patterns.

The 57.3-mm-diameter camera was used for routine identification of the samples, while the larger-diameter camera was used for the indexing of samples and the determination of the cell parameters.

3.3.2. The XRD Powder Patterns of Magnetite and Its Oxidation Products

The samples for powder analysis were ground to a few microns in particle size and approximately 1 mg of sample was poured into a glass capillary tube. The samples included magnetite prepared by reduction of hematite, magnetite prepared by precipitation from ferrous chloride solution, and RMB #5. The oxidation products of the reduced hematite and RMB #5 were also X-rayed following the DT tests. The XRD patterns of the three magnetite preparations are shown in Figure 4.3.1.

Each filled capillary was evacuated and melt-sealed to avoid oxidation or contamination by water vapour. The tube was centered in the cylindrical camera, rotated at 1 rpm, and exposed to the X-rays emitted from a cobalt X-ray tube. Electric input to the target was 33 kilovolts and 15 milliamperes. Cobalt was selected as target material because the "soft" radiation emitted from it, K_α = 1.7889 Å, was of sufficiently low energy to minimize absorption by the samples. Iron filters were used to absorb all spectral components except for the desired K_α lines.

Commercial photographic film in the Straumanis-type mounting was employed to record the diffraction patterns; 5-hr and 15-hr exposure times were allowed for the 57.3- and 114.6-mm diameter cameras, respectively. XRD line intensities were estimated visually. A film shrinkage factor was included in all interplanar-spacing calculations for each film exposure. The factor was determined by considering a pair of lines about each hole in the film, and averaging the readings for

such a pair. The difference between these two averages should have equalled 90 mm and 180 mm for cameras of diameters 57.3 and 114.6 mm, respectively. The percentage difference from these figures was the film shrinkage correction factor which was added to each individual line measurement. The line measurements were in turn used to determine the interplanar spacing and to calculate the cell-edges and 2θ-angles of the reaction components of interest.

3.3.3. Calculation of the Cell Parameters of Magnetite, Maghemite and Hematite

Until recently, the structures of magnetite and maghemite have been said to have the cubic spinel-type of crystal lattice. However, the occurrence of cation vacancies in the unit cell of maghemite, and the appearance of XRD reflections which should not appear for the spinel structure, leads one to the assumption of a lower symmetry, the tetragonal, for the mineral. In other words, the oxidation of magnetite upon heating leads to the transformation of the cubic structure of magnetite to the tetragonal of maghemite and thence to the hexagonal of hematite. The unit cell of the spinel structure, of which the maghemite substructure is a member, is shown in Figure 2.3.3.

The relationship of the cell-edges and -angles to the interplanar spacing of the minerals is given in Table 3.3.3. The cell parameters were determined by the use of a program written by Gabe[25] for a CDC 6400 computer. The measured interplanar spacings, or d-spacings, were compared to those calculated from the glancing angle θ as given by the Bragg Equation. The XRD powder patterns of RMB #5 and RMB #5 oxidized to 310 and 650°C in dry air are illustrated in Figure 4.3.2, while Tables 4.3.1, 4.3.2, and 4.3.3 list the measured and calculated d-spacing and their derived cell-edges.

TABLE 3.3.3

Calculation of Cell Parameters for Magnetite, Maghemite and Hematite

Mineral	Crystal System	Unit Cell			Equivalent of $\frac{1}{d^2_{hk\ell}}$
		Diagnostic Symmetry	Cell-edge Relationships	Angular Relationships	
Magnetite (Fe_3O_4)		4 threefold axes at $109^o28'$ to each other	$a=b=c$	$\alpha=\beta=\gamma=90^o$	$\frac{1}{a^2}(h^2 + k^2 + \ell^2)$
Maghemite (γ-Fe_2O_3)	tetragonal (supercell)	1 fourfold axis	$a=b\neq c$	$\alpha=\beta=\gamma=90^o$	$\frac{h^2 + k^2}{a^2} = \frac{\ell^2}{c^2}$
Hematite (α-Fe_2O_3)	hexagonal (rhombohedral subdivision)	1 threefold inversion axis	$a=b\neq c$	$\alpha=\beta=90^o$ $\gamma=120^o$	$\frac{4}{3a^2}(h^2 + hk + k^2) + \frac{\ell 2}{c^2}$

α, β, γ = interaxial angles between b and c, a and c, and a and b, respectively.

a, b, c = unit cell edges.

h, k, ℓ = Miller indices for magnetite and maghemite, Bravais indices for hematite.

$d_{hk\ell}$ = interplanar spacing.

3.4.1. The Infrared Absorption Spectrophotometer

A Beckman IR-12 spectrophotometer operating in the double-beam mode was used to obtain infrared spectra in the range 200 - 4000 cm^{-1}.

3.4.2. The Infrared Absorption Analysis of RMB #5 and Its Oxidation Products

XRD examination of the products of oxidation of magnetite by the three foregoing methods indicated that only RMB #5 possessed either the chemical purity and/or the physical properties necessary for its conversion to the maghemite phase. For these reasons, the infrared investigation will be confined to only RMB #5 and its oxidation products.

Before recording the infrared spectra of these materials, the samples, which had agglomerated because of their fineness and heat treatment, were reduced to finer than 5 microns by grinding in an agate mortar under acetone. Particle size was checked by microscopic examination during the grinding process.

In order to minimize light scattering within the mineral-matrix disks from which the infrared spectra were recorded, it was necessary that the refractive indices of the mineral and the matrix be as nearly identical as possible. For this reason thallous bromide (TlBr) was chosen as the matrix because its refractive index is between 2.4 and 2.8, whereas that of magnetite is 2.42, maghemite between 2.52 and 2.74, and hematite 3.22ω, 2.94ε (Na D). A second advantage of TlBr was its non-hygroscopic nature which minimized adsorption of extraneous atmospheric moisture during preparation and spectral recording.

Sample disks were composed of 0.25 wt. per cent mineral in TlBr to a total disk wt. of 250 mg. The matrix-mineral combination was vigorously mixed by vibration on a "Wig-l-bug" for 5 minutes, and the 250-mg mixture was

then pressed into 0.5 inch diameter circular disks at 25,000 psig for 5 minutes under vacuum.

The infrared absorption spectra of the disks were recorded against a 250-mg TlBr reference under the following conditions:

Nernst glower current - 0.60 ampere;

scanning speed - 40 cm^{-1}/min;

gain - 3%;

period - 8 sec;

single beam/double beam ratio - 1:1;

ordinate scale - 0 to 1 absorbance;

frequency range - 200 to 4,000 cm^{-1}; and

slit width - variable.

The resultant spectral absorption frequencies and the maximum DTA oxidation temperatures to which the samples were subjected are listed in Tables 4.4.1 and 4.4.2 for the dry and wet oxidation respectively, and the corresponding spectra are shown in Figures 4.4.1 and 4.4.2.

In order to separate quantitatively the spectral absorption peaks from the neighbouring peaks, a Dupont Peak Resolver 310 was used. Each oscilloscope pattern of the resolver channels was matched with a standard Lorentzian-type absorption curve. Then, by adjustment of the position, height, and width of the individual oscilloscope pattern to the position, height, and width of the consecutive infrared peaks, the composition of overlapping peaks and shoulders was resolved, and the pattern of each channel was separately recorded on the spectral curve immediately below the "real" curve. The real curve then equalled the sum of the intensity contributions of each of the resolved peaks, at that particular frequency. An example of such a

resolved spectrum from the present study is presented in Figure 4.4.4.

There was no physical basis for assuming a Lorentzian peak shape in the present study other than the fact that infrared absorptions often assume such a shape with a horizontal baseline. The shape occurs because the Beer-Lambert-Bouguer Law is not strictly obeyed since the spectrophotometer exit slit has a finite width which allows a narrow distribution of frequencies in close proximity to the peak frequency to pass to the detector. This results in artificial broadening of the recorded peak. For a single symmetrical absorption peak:

$$a(\omega) = \frac{A}{\pi}\left(\frac{\gamma}{(\omega-\omega_o)^2 + \gamma^2}\right) \qquad (3.4.2.)$$

where: $a(\omega)$ = absorption coefficient at ω,

ω = frequency,

ω_o = frequency of absorption maximum,

A = integrated intensity or total absorption of energy for the mode occurring at frequency ω,

γ = peak half-width. This property is independent of the inherent strength of the absorption peak. When $\omega-\omega_o = \gamma$, the absorption coefficient has half the value it has at ω_o.

An absorption having the symmetrical shape of the function described by Equation 3.4.2 is said to be Lorentzian.

CHAPTER 4

EXPERIMENTAL RESULTS

4.1. Preparation of Magnetite

Table 4.1 summarizes the preparative conditions used in synthesizing magnetite and lists some of the analytical results measured from the synthetic preparations. For the method employing precipitation from ferrous chloride solution, each change of pH, gas-flow rate or gas-flow period meant a new preparation under the new condition.

4.2. DT and Thermogravimetric (TG) Analyses

The DT curves resulting from the oxidation of reduced hematite and of RMB #5 are presented in Figures 4.2.1 and 4.2.2, respectively, while Figure 4.2.3 shows the thermogravimetric analysis curve for RMB #5 in a flowing helium atmosphere.

4.3. XRD Measurements

The XRD powder patterns of the reduced hematite, the ferrous chloride precipitation product, and RMB #5 are shown in Figure 4.3.1. The patterns for the oxidation products of RMB #5 taken to temperatures of 310 and 650^{o}C in dry air are shown in Figure 4.3.2(b) and (c), respectively. The derived interplanar spacings of RMB #5 and its oxidation products at the above temperatures are presented in Tables 4.3.1, 4.3.2, and 4.3.3. For comparison, also given are the d-spacings and cell edges determined from the powder work of Basta[26], Haul and Schoon[13], and Pauling and Hendricks[16] for magnetite, maghemite and hematite, respectively. The calculated d-spacings

were determined from Equation 2.3.2, and the cell edges for the different crystal systems were calculated from the formulas of Table 3.3.3. It should be noted that the d-spacings in Tables 4.3.1, 4.3.2, and 4.3.3. were determined from the powder patterns of the 114.6 mm camera, while the contact prints of Figures 4.3.1 and 4.3.2 are those of the 57.3 mm camera.

The powder pattern of Figure 4.3.2 (b) and Table 4.3.2 is that of maghemite containing a suspected very small trace of both magnetite and hematite. The diffraction lines characteristic of the spinel structure to which magnetite belongs are identified by an "s", while the lines possibly belonging to hematite are shown by an asterisk (*).

TABLE 4.1

Reaction Parameters and Product Properties of Magnetite Preparations

Reaction Parameter	Hematite (α-Fe_2O_3) Reduction	Ferrous Chloride ($FeCl_2.4H_2O$) Oxid.	Magnetite-Goethite (Fe_3O_4-$Fe_2O_3.H_2O$), or Mapico Black (MB) Reduction					
			MB	RMB #1	RMB #2	RMB #3	RMB #4	RMB #5
Reduction Temp. (°C)	1100	--- --- ---	---	800	800	800	800	400
Oxidation Temp. (°C)	---	Room Temp (22°C)	---	---	---	---	---	---
Red. or Oxid. Gas (V%)	H_2/CO_2 10/90	Compressed Air	---	CO/CO_2 9.2/90.8			10.6/89.4	
Red. or Oxid. Time (hr)	18	0.5 - 5.0 in 0.5 hr increments	---	6	8	12	8	3
Gas Flow Rate (ℓ/min)	0.3	10^{-3}, 10^{-2}, 1.5×10^{-1}	---	0.5	0.75	0.5	1.0	2.0
Solution pH	---	8.5, 11.0, 12.8	---	---	---	---	---	---
Sample Weight (g)	18.1925	approx. 17 g/trial	---	12.8413	13.7673	15.8884	12.5599	28.3745
Red. or Oxid. Wt. (g)	17.5093	--- --- ---	---	12.5164	13.3298	15.4361	12.1578	27.6353
Weight Change (%)	-3.25	--- --- ---	---	-2.53	-3.18	-2.84	-3.29	-2.62
Product Properties								
Specific Surface (m^2/g)	0.4	69.7 @pH 11, oxid. 3 hr, flow 1.5×10^{-1} ℓ/min	10.3	5.2	0.9	---	0.7	6.2
Fe Total (%)	---	--- --- ---	67.29	71.16±0.06	---	---	71.37±0.05	71.49±0.08
Fe^{2+} (%)	---	--- --- ---	16.22	22.63±0.04	---	---	22.95±0.03	22.97±0.04
Fe^{3+}	---	--- --- ---	51.07	48.53±0.10	---	---	48.42±0.08	48.52±0.12
Stoichiometric Fe^{2+} (%)			24.12					
Stoichiometric Fe^{3+} (%)			48.24					

--- not determined or inapplicable

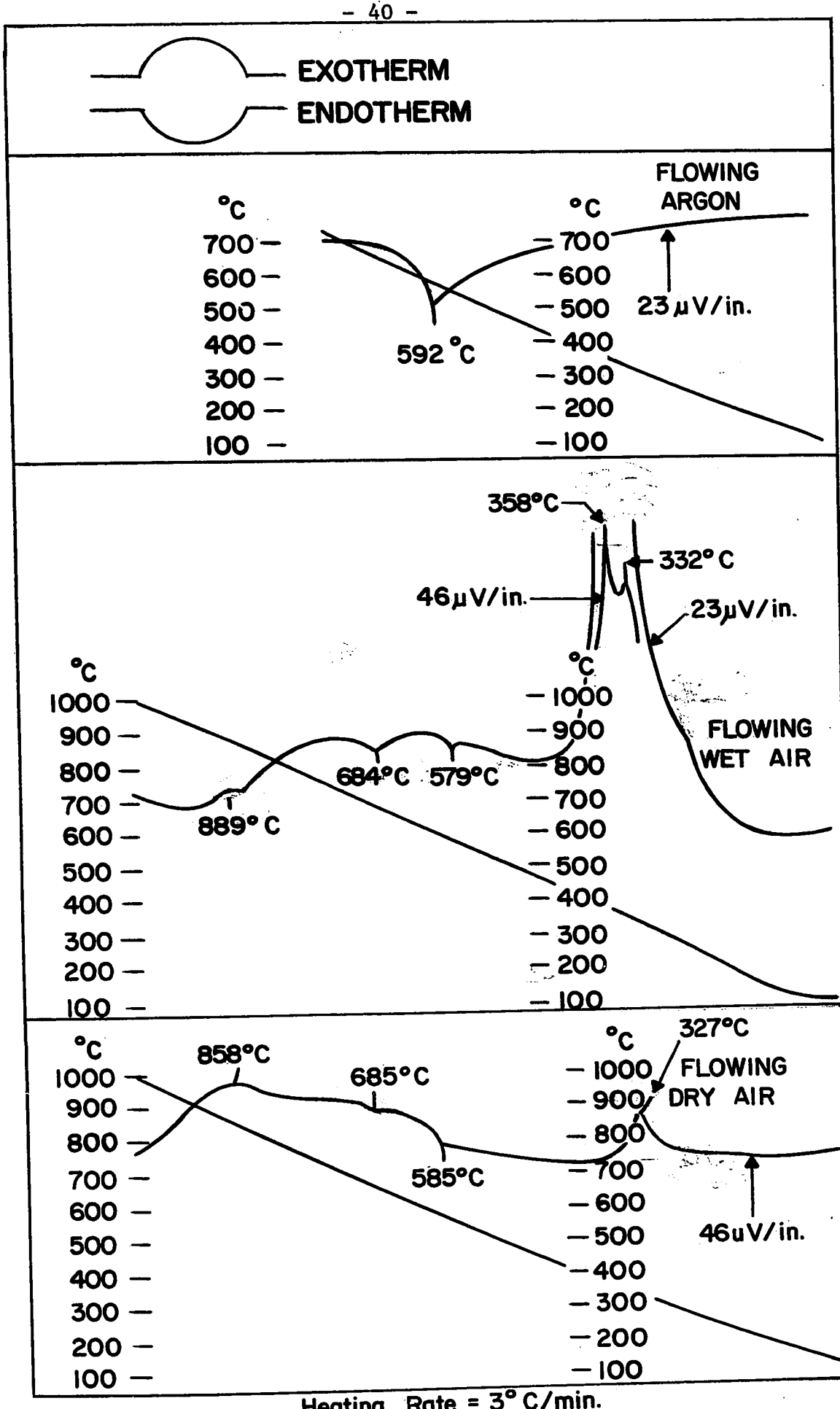

Heating Rate = 3° C/min.

FIGURE 4.2.1 DTA of Reduced Hematite in Flowing Argon, Wet Air, and Dry Air

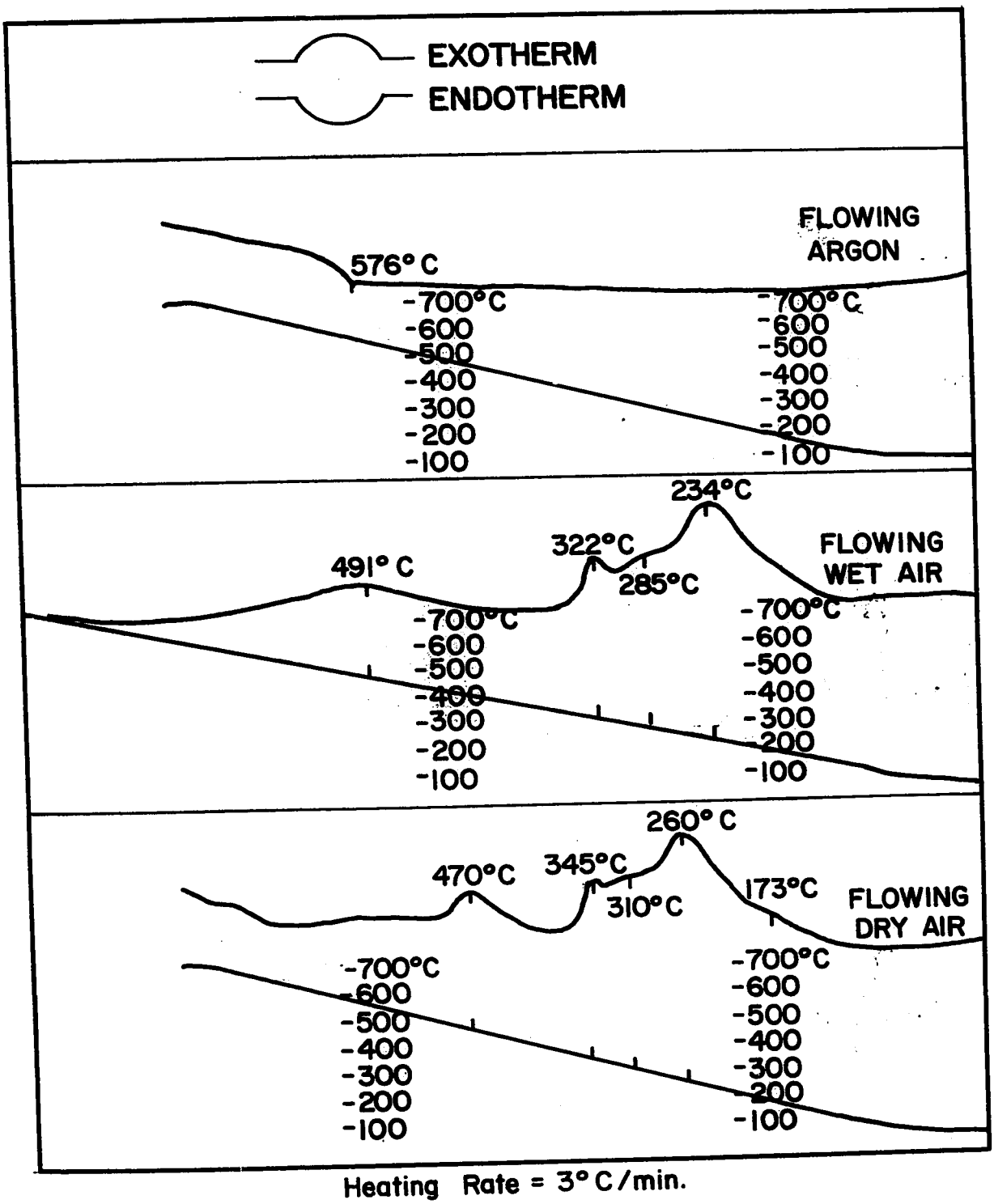

Figure 4.2.2 DTA of RMB #5 in Flowing Argon, Wet Air, and Dry Air
Sensitivity = 40 μV/ in.

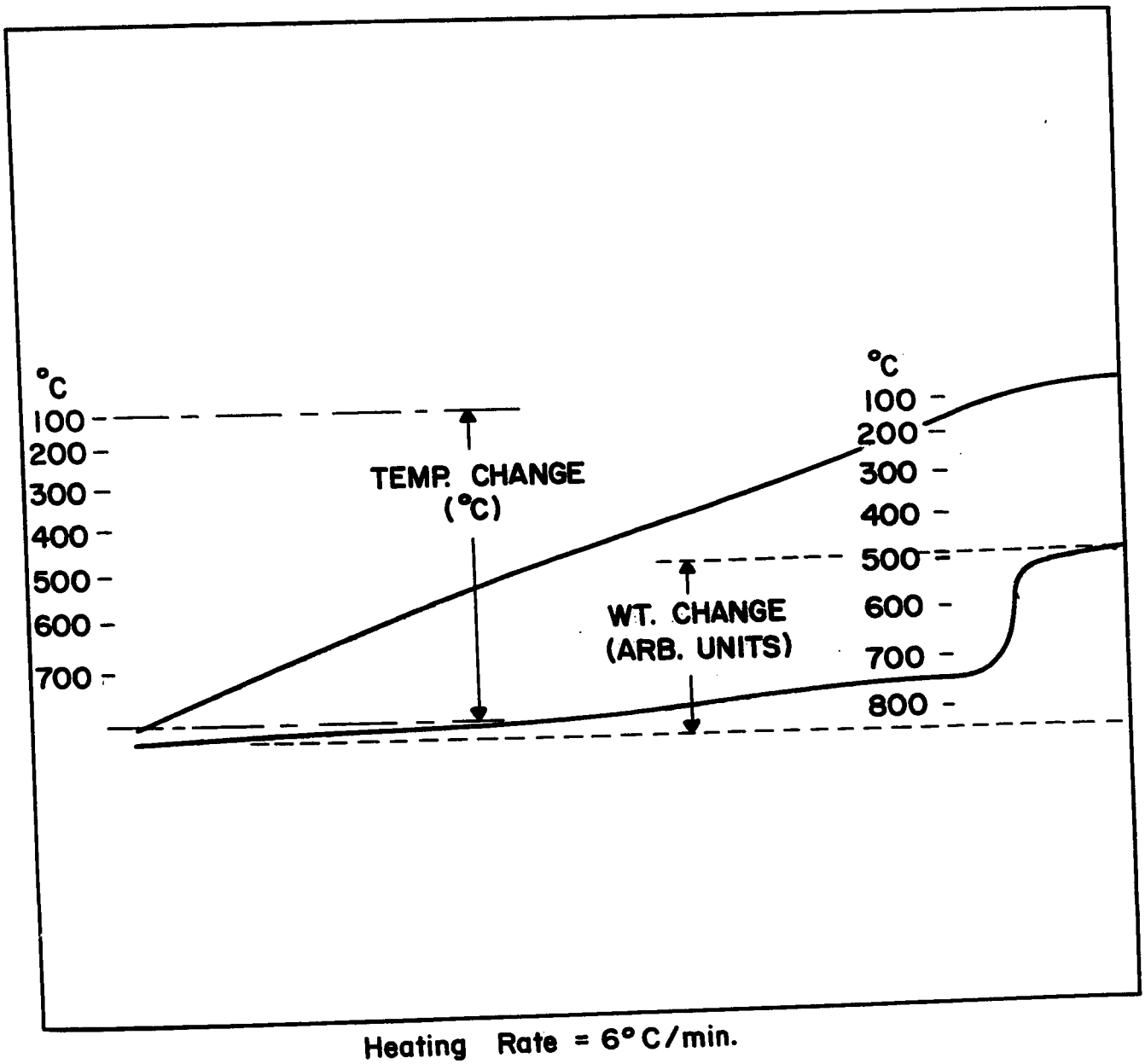

FIGURE 4.2.3 TGA of RMB #5 to 800° C in Flowing Helium

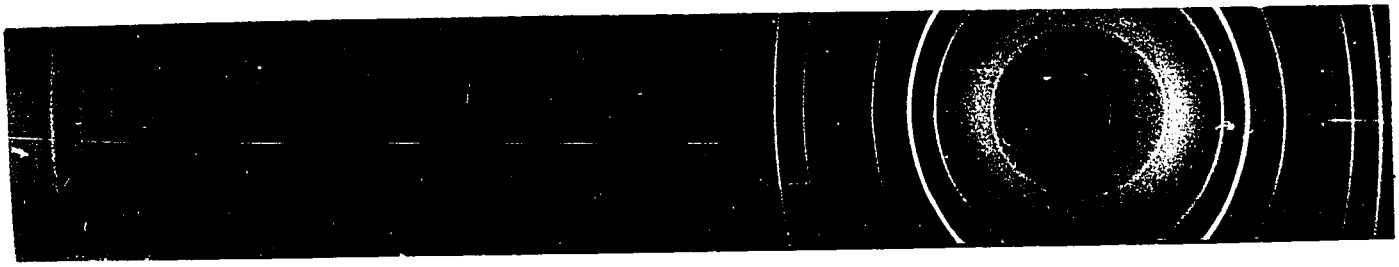

(a) Reduced Hematite

(b) Ferrous Chloride Precipitation Product

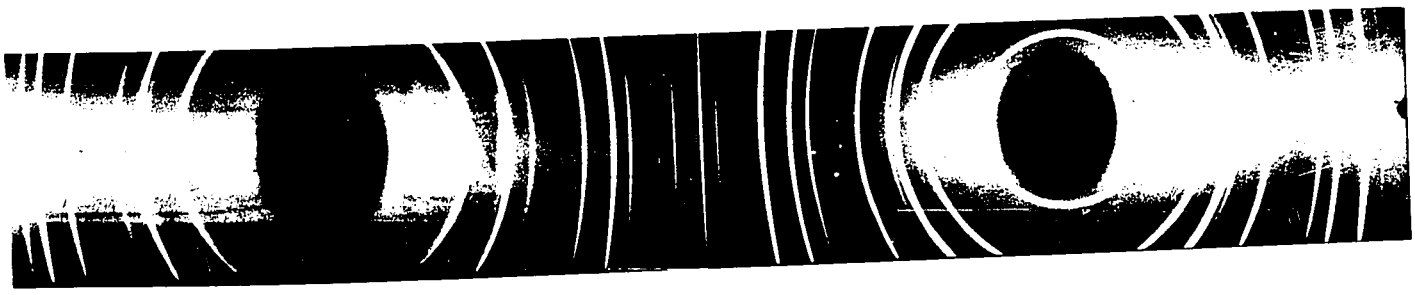

(c) RMB #5

FIGURE 4.3.1. X-ray Powder Contact Prints of Reduced Hematite, Ferrous Chloride Precipitation Product, and RMB #5. Filtered Co Radiation, camera diameter = 57.3 mm.

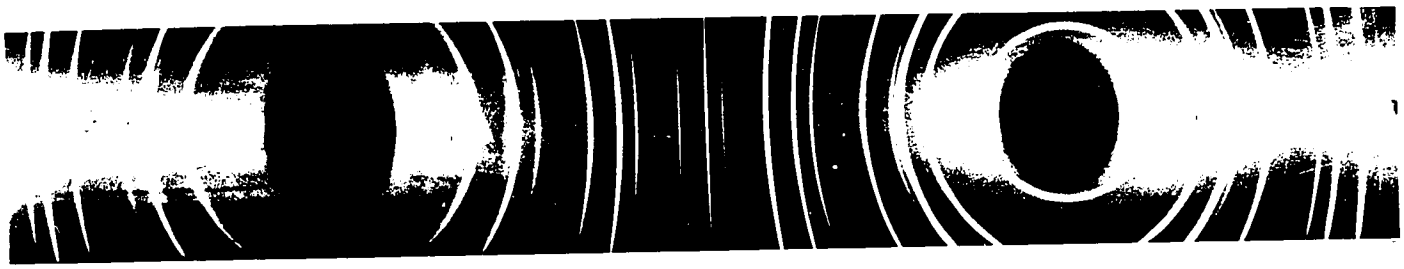

(a) RMB #5

(b) RMB #5 to 310°C in dry air

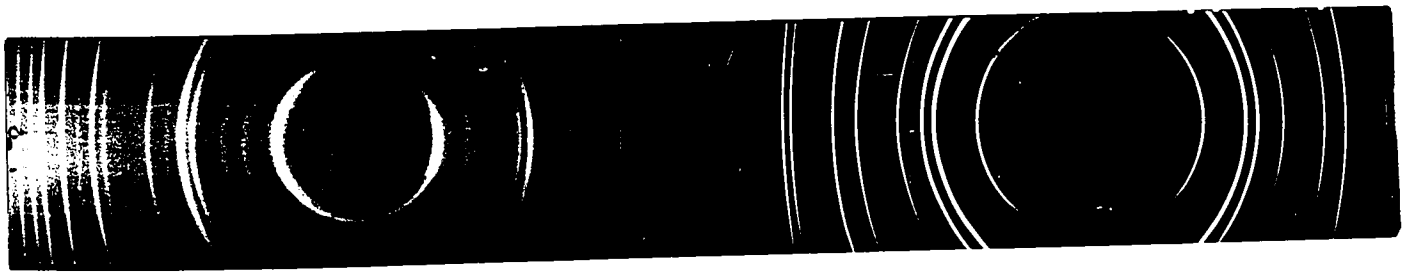

(c) RMB #5 to 650°C in dry air

FIGURE 4.3.2. X-ray Powder Contact Prints of RMB #5 and Its Oxidation Products Heated to 310 and 650°C in dry air.

TABLE 4.3.1

INTERPLANAR SPACING AND MILLER INDICES FOR RMB #5

I = visually estimated diffraction pattern intensity (arbitrary units)

d_{obs}, d_{calc} = observed and calculated interplanar spacing, respectively

h,k,ℓ = Miller indices

RMB #5				Ref. 26 - Natural Fe_3O_4		
d_{obs} (Å)	h k ℓ	d_{calc} (Å)	I	d_{obs} (Å)	h k ℓ	I
4.849	1 1 1	4.846	40	4.85	1 1 1	40
2.971	2 2 0	2.968	60	2.966	2 2 0	70
2.531	3 1 1	2.531	100	2.530	3 1 1	100
2.421	2 2 2	2.423	20	2.419	2 2 2	10
2.097	4 0 0	2.098	50	2.096	4 0 0	70
1.712	4 2 2	1.713	40	1.712	4 2 2	60
1.614	3 3 3 5 1 1	1.615	60	1.614	3 3 3 5 1 1	85
1.483	0 4 4	1.484	80	1.483	4 4 0	85
1.418	5 3 1	1.419	10			
1.327	6 2 0	1.327	30	1.327	6 2 0	20
1.280	5 3 3	1.280	40	1.279	5 3 3	30
1.265	6 2 2	1.265	20	1.264	6 2 2	10
1.211	4 4 4	1.212	40	1.2112	4 4 4	20
1.176	7 1 1	1.175	0.5			
1.121	6 4 2	1.122	40	1.1214	6 4 2	30
1.092	5 5 3 7 3 1	1.093	60	1.0922	5 5 3 7 3 1	60
1.051	8 0 0	1.049	50	1.0489	8 0 0	40
0.989	6 6 0 8 2 2	0.989	20	0.9890	6 6 0 8 2 2	10
0.969	5 5 5 7 5 1	0.969	50	0.9692	5 5 5 7 5 1	40
0.963	6 6 2	0.962	10			
0.938	8 4 0	0.938	30	0.9386	8 4 0	30
CUBIC SYSTEM:				CUBIC SYSTEM:		
a=b=c=8.393±0.004 Å α=β=γ=90.00°				a=b=c=8.3963 Å α=β=γ=90.00°		

TABLE 4.3.2

INTERPLANAR SPACING AND MILLER INDICES FOR THE OXIDATION PRODUCT OF RMB #5 TO 310°C

I = visually estimated diffraction pattern intensity
I_A = diffraction pattern intensity from diffractometer
lines denoted "s" = those of spinel structure
* = possible trace of hematite (α-Fe_2O_3)

RMB #5 Oxidized to 310°C				Ref. 13 - Synthetic γ-Fe_2O_3		
d_{obs} (Å)	h k ℓ	d_{calc} (Å)	I	d_{obs} (Å)	h k ℓ	I_A
8.01	1 0 1	7.90	10	8.02	1 0 1	8
6.89	1 0 2	6.93	10	7.04	1 0 2	18
				6.35	0 0 4	8
5.87	1 1 0 1 0 3	5.89	30	5.95	1 1 0 1 0 3	60
				5.75	1 1 1	4
5.32	1 1 2	5.33	5	5.37	1 1 2	8
				5.00	0 0 5 1 0 4	8
4.81 s	1 1 3 s	4.81 s	30 s	4.84 s	1 1 3 s	40 s
4.29	1 1 4 1 0 5	4.28	5	4.32	1 1 4 1 0 5	25
				4.13	0 0 6 2 0 0	2
				3.86	1 1 5	12
3.72	2 0 3 1 0 6	3.72	30	3.75	2 0 3 1 0 6	100
				3.50	2 0 4	12
3.39	1 1 6 2 1 3	3.40	30	3.42	1 1 6 2 1 3	65
3.21	2 0 5 2 1 4	3.20	10	3.216	2 0 5 2 1 4	25
				3.077	1 1 7	2
2.95 s	2 2 0 2 0 6 s	2.95 s	70 s	2.950 s	2 2 0 2 0 6 s	100 + s
2.86	2 2 2	2.86	5	2.871	2 2 2	<1
2.77	3 0 0 0 0 9	2.77	10	2.799	3 0 0 0 0 9	18
2.70*	2 0 7*	2.71*	10*			
2.63	3 0 3 3 1 0	2.63	10	2.642	3 0 3 3 1 0	25

(Continued)

(Table 4.3.2. continued)

RMB #5 Oxidized to 310°C				Ref. 13 - Synthetic γ-Fe_2O_3		
d_{obs} (Å)	h k ℓ	d_{calc} (Å)	I	d_{obs} (Å)	h k ℓ	I_A
2.52*s	3 1 3 *s 1 1 9	2.51*s	100*s	2.521 s	3 1 3 s 1 1 9	100 + s
				2.451	3 1 4 3 0 5	<1
2.41 s	2 2 6 s	2.40 s	5 s	2.414 s	2 2 6 s	8 s
2.31	3 2 0 3 0 6	2.31	10	2.318	3 2 0 3 0 6	8
				2.234	2 1 9 3 1 6	4
2.20	3 0 7	2.19	5	2.208	3 0 7	4
2.08 s	4 0 0 s	2.08 s	50	2.089 s	4 0 0 s	100 + s
				2.026	4 1 0 4 0 3	<1
				1.994	4 1 2	<1
				1.967	3 3 0 3 0 9	<1
				1.863	4 2 0 4 0 6	2
				1.836	4 4 2	1
1.814*	4 2 3 * 4 1 6	1.819*	10*	1.822	4 2 3 4 1 6	16
				1.778	3 3 6	1
				1.749	4 2 5	1
1.701*s	4 2 6*s	1.701*s	40*s	1.702 s	4 2 6 s	100 + s
1.669	4 0 9 5 0 0	1.667	5	1.669	4 0 9 5 0 0	8
				1.638	5 0 3 5 1 0	4
1.605 s	3 3 9 s 5 1 3	1.604 s	50 s	1.608 s	3 3 9 s 5 1 3	100 + s
1.544	2 5 1	1.545	10	plus 24 additional reflections down to 1.068		
1.520	2 5 3	1.522	10			
1.475 s	4 4 0 s 2 5 5	1.478 s	60 s	TETRAGONAL SYSTEM:		
1.322 s	1 6 5 s	1.321 s	30 s	a=b=8.33 Å, c=24.99 Å		
1.273 s	1 6 7 s	1.279 s	40 s	$\alpha=\beta=\gamma=90.00^\circ$		
1.256 s	2 6 6 s	1.256 s	5 s			
1.201 s	4 5 8 s	1.201 s	20 s			

(Continued)

(Table 4.3.2. continued)

RMB #5 Oxidized to 310°C				Ref. 13 - Synthetic γ-Fe_2O_3		
d_{obs} (Å)	h k ℓ	d_{calc} (Å)	I	d_{obs} (Å)	h k ℓ	I_A
1.113 s	0 7 8 s	1.112 s	20 s			
1.086 s	{ 5 5 3 / 1 7 9 } s	1.085 s	40 s			
1.042 s	0 8 0 s	1.042 s	20 s			
0.9832 s	2 8 6 s	0.9824 s	10 s			
0.9632	5 7 3	0.9626	40			
0.9332	4 8 0	0.9320	10			

TETRAGONAL SYSTEM:

a=b=8.336±0.001 Å, c=25.015±0.001 Å

$\alpha=\beta=\gamma=90.00^{\circ}$

TABLE 4.3.3.

INTERPLANAR SPACING AND MILLER INDICES FOR THE OXIDATION PRODUCT OF RMB #5 TO 650°C

I = visually estimated diffraction pattern intensity
I_B = recording microphotometer diffraction pattern intensity

RMB #5 Oxidized to 650°C					Ref. 16 - Natural α-Fe_2O_3				
d_{obs} (Å)	h k i ℓ	h k ℓ	d_{calc} (Å)	I	d_{obs} (Å)	h k i ℓ	h k ℓ	d_{calc} (Å)	I_B
3.68	0 1 $\bar{1}$ 2	1 1 0	3.67	4	3.68	0 1 $\bar{1}$ 2	1 1 0	3.685	3
2.69	1 0 $\bar{1}$ 4	2 1 1	2.69	10	2.69	1 0 $\bar{1}$ 4	2 1 1	2.701	10
2.51	1 1 $\bar{2}$ 0	1 0 $\bar{1}$	2.51	7	2.52	1 1 $\bar{2}$ 0	1 0 $\bar{1}$	2.520	8
2.20	1 1 $\bar{2}$ 3	2 1 0	2.20	4	2.21	1 1 $\bar{2}$ 3	2 1 0	2.208	4
2.07	2 0 $\bar{2}$ 2	2 0 0	2.07	1	2.09	2 0 $\bar{2}$ 2	2 0 0	2.080	½
1.837	0 2 $\bar{2}$ 4	2 2 0	1.837	4	1.843	0 2 $\bar{2}$ 4	2 2 0	1.843	6
1.692	1 1 $\bar{2}$ 6 2 1 $\bar{3}$ 1	3 2 $\bar{1}$ 2 0 $\bar{1}$	1.691 1.63	8	1697 1.638	1 1 $\bar{2}$ 6 2 1 $\bar{3}$ 1	3 2 $\bar{1}$ 2 0 $\bar{1}$	1.695 1.637	7 ½
1.597	1 2 $\bar{3}$ 2 0 1 $\bar{1}$ 8	2 1 $\bar{1}$ 3 3 2	1.6006 1.597	3	1.604	1 2 $\bar{3}$ 2 0 1 $\bar{1}$ 8	2 1 $\bar{1}$ 3 3 2	1.604 1.600	3
1.484	2 1 $\bar{3}$ 4	3 1 0	1.482	5	1.488	2 1 $\bar{3}$ 4	3 1 0	1.487	5
1.451	0 2 $\bar{2}$ 7 3 0 $\bar{3}$ 0	3 3 $\bar{1}$ 2 1 $\bar{1}$	1.457 1.451	5	1.457	0 2 $\bar{2}$ 7 3 0 $\bar{3}$ 0	3 3 $\bar{1}$ 2 1 $\bar{1}$	1.460 1.455	5
1.348	2 0 $\bar{2}$ 8	4 2 2	1.348	2	1.351	2 0 $\bar{2}$ 8	4 2 2	1.351	1
1.310	1.0.1.10	4 3 3	1.310	5	1.313	1.0.1.10	4 3 3	1.313	4
1.257	2 1 $\bar{3}$ 7 2 2 $\bar{4}$ 0	4 2 $\bar{1}$ 2 0 $\bar{2}$	1.261 1.257	3	1.261	2 1 $\bar{3}$ 7 2 2 $\bar{4}$ 0	4 2 $\bar{1}$ 2 0 $\bar{2}$	1.264 1.260	2
1.227	3 0 $\bar{3}$ 6	4 1 1	1.225	1	1.233	3 0 $\bar{3}$ 6	4 1 1	1.228	½
1.212	2 2 $\bar{4}$ 3	3 1 $\bar{1}$	1.212	1	1.215	2 2 $\bar{4}$ 3	3 1 $\bar{1}$	1.214	½
1.188	3 1 $\bar{4}$ 2 1 2 $\bar{3}$ 8	3 0 $\bar{1}$ 4 3 1	1.189 1.187	1	1.192	3 1 $\bar{4}$ 2 1 2 $\bar{3}$ 8	3 0 $\bar{1}$ 4 3 1	1.192 1.190	2
1.161	0.2.2.10	4 4 2	1.161	1	1.166	0.2.2.10	4 4 2	1.162	2
1.139	1 3 $\bar{4}$ 4	3 2 $\bar{1}$	1.139	3	1.143	1 3 $\bar{4}$ 4	3 2 $\bar{1}$	1.141	4
1.101	2 2 $\bar{4}$ 6	4 2 0	1.101	4	1.106	2 2 $\bar{4}$ 6	4 2 0	1.104	4
1.074	0 4 $\bar{4}$ 2	2 2 $\bar{2}$	1.075	1	1.079	0 4 $\bar{4}$ 2	2 2 $\bar{2}$	1.077	½
1.054	2.1.3.10	5 3 2	1.054	4	1.058	2.1.3.10	5 3 2	1.056	5
1.037	4 0 $\bar{4}$ 4	4 0 0	1.036	2	1.042	4 0 $\bar{4}$ 4	4 0 0	1.040	1

(...cont'd)

(Table 4.3.3. Continued)

RMB #5 Oxidized to 650°C					Ref. 16 - Natural α-Fe_2O_3				
d_{obs} (Å)	h k i ℓ	h k ℓ	d_{calc} (Å)	I	d_{obs} (Å)	h k i ℓ	h k ℓ	d_{calc} (Å)	I_B
0.9888	2 3 $\bar{5}$ 2 3 1 $\bar{4}$ 8	3 1 $\bar{2}$ 5 2 1	0.9887 0.9878	3	0.990	2 3 $\bar{5}$ 2 3 1 $\bar{4}$ 8	3 1 $\bar{2}$ 5 2 1	0.991 0.990	3
0.9598	2 3 $\bar{5}$ 4	5 4 5	0.9576	4					
0.9510	1 4 $\bar{5}$ 0	5 1 1	0.9508	3					
0.9310	1 4 $\bar{5}$ 3	3 2 2	0.9350	1					
0.9191	4 0 $\bar{4}$ 8	4 4 0	0.9185	1					
0.9080	3.1.$\bar{4}$.10	5 4 1	0.9064	3					

HEXAGONAL SYSTEM:
$a=b=5.029\pm0.001$ Å
$c=13.731\pm0.004$ Å
$\alpha=\beta=90^0$, $\gamma=120^0$

HEXAGONAL SYSTEM:
$a=b=5.039$ Å, $c=13.76$ Å
$\alpha=\beta=90^0$, $\gamma=120^0$

4.4. Infrared Absorption Analysis of RMB #5 And Its Oxidation Products

Of all the preparative attempts, only that of RMB #5 produced magnetite of sufficient purity and reactivity to encourage further investigation by infrared absorption analysis. For this reason, the infrared study will be confined to only RMB #5 and its oxidation products.

The spectral data are presented in Tables 4.4.1 and 4.4.2 for the anhydrous and wet oxidation of RMB #5, respectively. The gradual changes in these spectra with increasing reaction temperature can be seen by examining Figures 4.4.1 and 4.4.2, respectively. For comparison, Figure 4.4.3 shows the spectra of the dry samples immediately below those of the wet samples recorded after oxidation to the same temperature. It should be noted that the spectra of Figures 4.4.1 to 4.4.3 and the corresponding Tables 4.4.1 and 4.4.2 apply to the unresolved spectra as recorded directly by the spectrophotometer.

However, Figure 4.4.4 shows an example of a spectrum in which the 325°C wet oxidation product of RMB #5 was recorded and resolved by the Dupont Peak Resolver. The resolved peak heights for the fundamental absorptions are indicated on the diagram, and an attempt was made to employ these peak heights in the calculation of activation energies as outlined in the Theory.

To aid in the assignment of the infrared absorption fundamentals, bondscan analyses for magnetite, maghemite and hematite are listed in Table 4.4.3. The assignments for the three minerals are given in Table 4.4.4.

It should be noted that the curves given in Figures 4.4.1 and 4.4.2 have undergone a several-fold size reduction and consequently are not to be taken as quite accurate. In some cases, minor spectral features are not apparent from these reduced curves.

FIGURE 4.4.1 Infrared Absorption Spectra of RMB #5 and it's Dry Air Oxidation Products at Selected Temperatures.

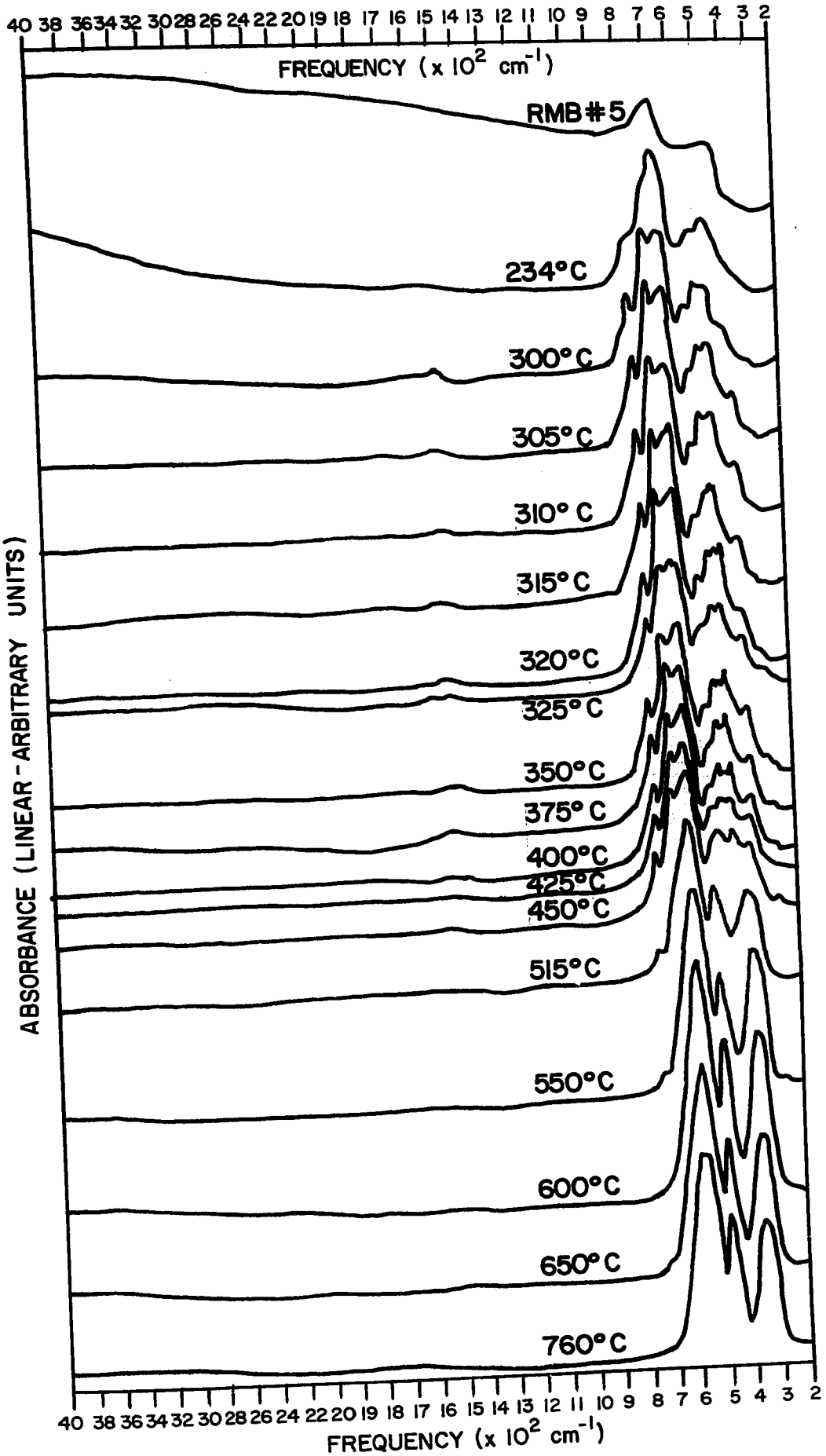

TABLE 4.4.1

Infrared Spectra of Reduced Mapico Black (RMB) #5 and its Products Formed at 3°C/min Temperature Elevation in Flowing Dry Air

(Figures in Frequency Columns Denote Peak Height from Baseline)
(sh = shoulder)

Sample	Absorption Frequencies (cm^{-1})											XRD Analysis (a = unit cell edge)
	320	345	400	420	450	480	570	590	630	700	1450	
RMB #5			26					51		sh18		Magnetite only (a = 8.393 Å)
234°C			28		sh24			54		sh20	3	Magnetite + minor maghemite
300°C	sh18		33	34	35	sh27	57	57	58	32	3	Maghemite + minor magnetite
305°C	24		44	43	44	sh32	67	sh64	68	38	3	Maghemite (a = 8.336 Å) + very small trace (hematite and magnetite)
310°C	27		48	47	47	sh35	67	67	70	40	4	Maghemite (a = 8.336 Å) + very small trace (hematite and magnetite)
315°C	27		47	46	46	sh35	73	70	71	40	4	Maghemite (a = 8.331 Å) + very small trace (hematite and magnetite)
320°C	27		55	53	53	sh42	78	76	79	43	4	Maghemite (a = 8.349 Å) + small minor hematite
325°C	23		36	35	35	sh27	53	55	53	31	3	Maghemite (a = 8.352 Å) + small minor hematite
350°C	28		43	39	40	sh30	64	63	61	33	2	Maghemite (a = 8.343 Å) + small minor hematite
375°C	28		44	41	43	sh32	64	65	66	38	2	Maghemite (a = 8.339 Å) + small minor hamatite
400°C	30		42	41	43	sh34	69	sh65	65	36	3	Maghemite (a = 8.351 Å) + small minor hematite
425°C	29		36	34	37	sh31	59		56	30	1	Maghemite + small minor hematite
450°C	32		37	sh34	37	sh34	62		55	30	2	Maghemite + minor hematite
515°C		36				38	66			15		Hematite + minor maghemite
550°C		60				51	85			sh12		Hematite + minor maghemite
600°C		72				69	100			sh11		Hematite + large trace maghemite
650°C		61				58	87			sh 9		Hematite only (a_{hex} = 5.029 Å)
760°C		56				60	85			sh 9		Hematite only

FIGURE 4.4.2 Infrared Absorption Spectra of RMB # 5 and it's Wet Air Oxidation Products at Selected Temperatures

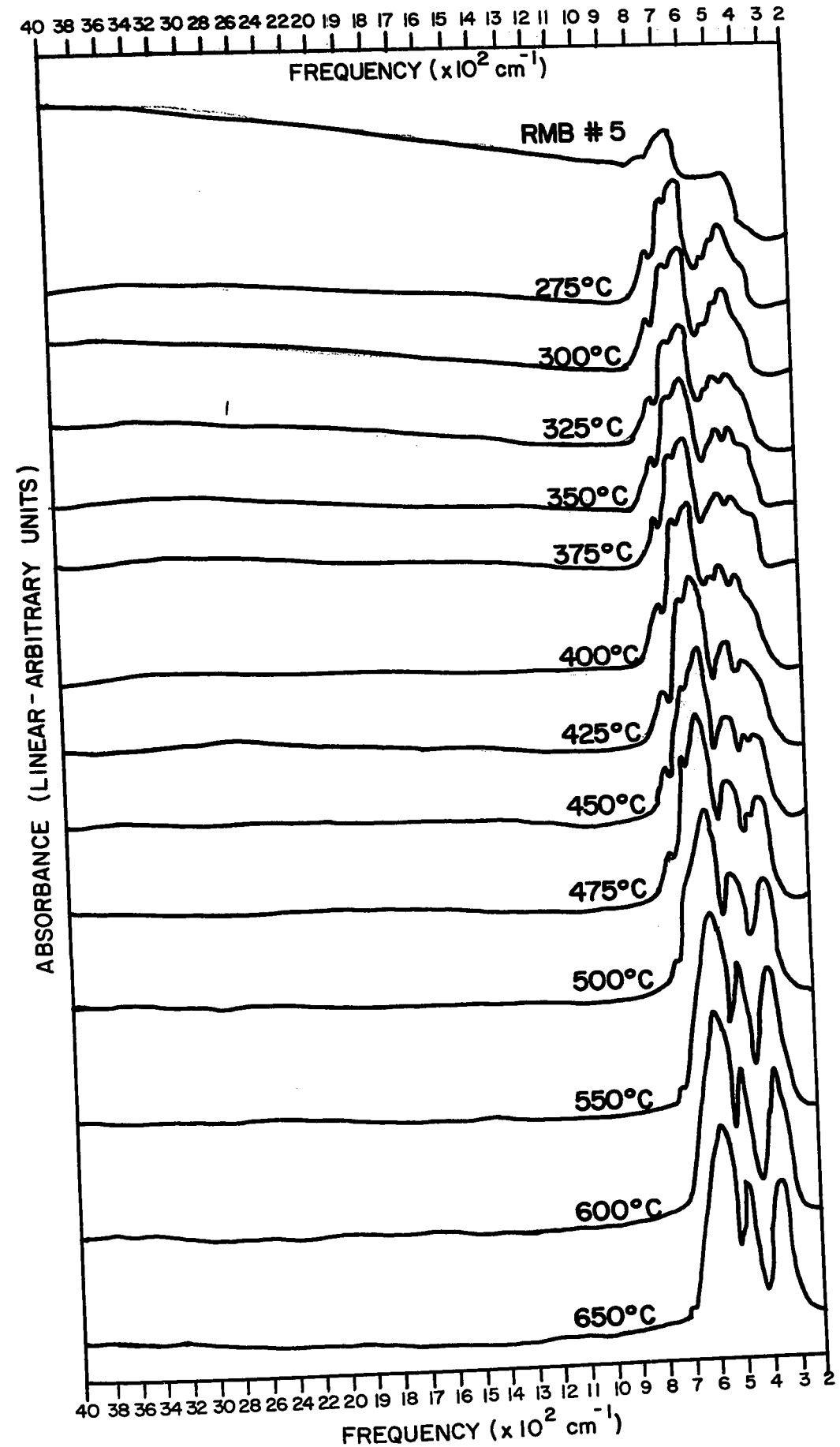

TABLE 4.4.2

Infrared Spectra of Reduced Mapico Black (RMB) #5 and its Products Formed at 3°C/min Temperature Elevation in Flowing Wet Air

(Figures in Frequency Columns Denote Peak Heights from Baseline)
(sh = shoulder)

Sample	Absorption Frequencies (cm^{-1})											XRD Analysis
	320	345	400	420	450	480	570	590	630	700	1450	
RMB #5			26					51		sh18		Magnetite only (a = 8.393 Å)
275°C	sh16		34	sh30	27	sh19	50	sh49	42	23	2	Maghemite + minor magnetite
300°C	sh18		35	sh31	30	sh20	53	sh48	43	24	2	Maghemite + minor magnetite
325°C	sh19		29	sh25	29	sh22	49	sh48	42	20	6	Maghemite + minor hematite + small trace magnetite
350°C	sh26		34	sh29	33	sh26	55	55	47	22	6	Maghemite (a = 8.321 Å) + minor hematite
375°C	sh24		31	sh27	33	sh26	54	54	47	21	6	Maghemite + minor hematite
400°C	sh25		38	sh35	42	sh36	68	sh66	62	27	3	Approximately equal maghemite + hematite
425°C	sh28		36	sh32	42	sh37	69	sh64	58	23	4	Approximately equal maghemite + hematite
450°C	sh30	35	34		40	sh38	68	sh64	54	21		Approximately equal maghemite + hematite
475°C		45	sh35			49	78		sh56	21		Hematite + minor maghemite
500°C		48				50	75		sh54	15		Hematite + minor maghemite
550°C		57				60	83			sh11		Hematite + small minor maghemite
600°C		62				63	86			sh10		Hematite + trace maghemite
650°C		60				62	84			sh10		Hematite only

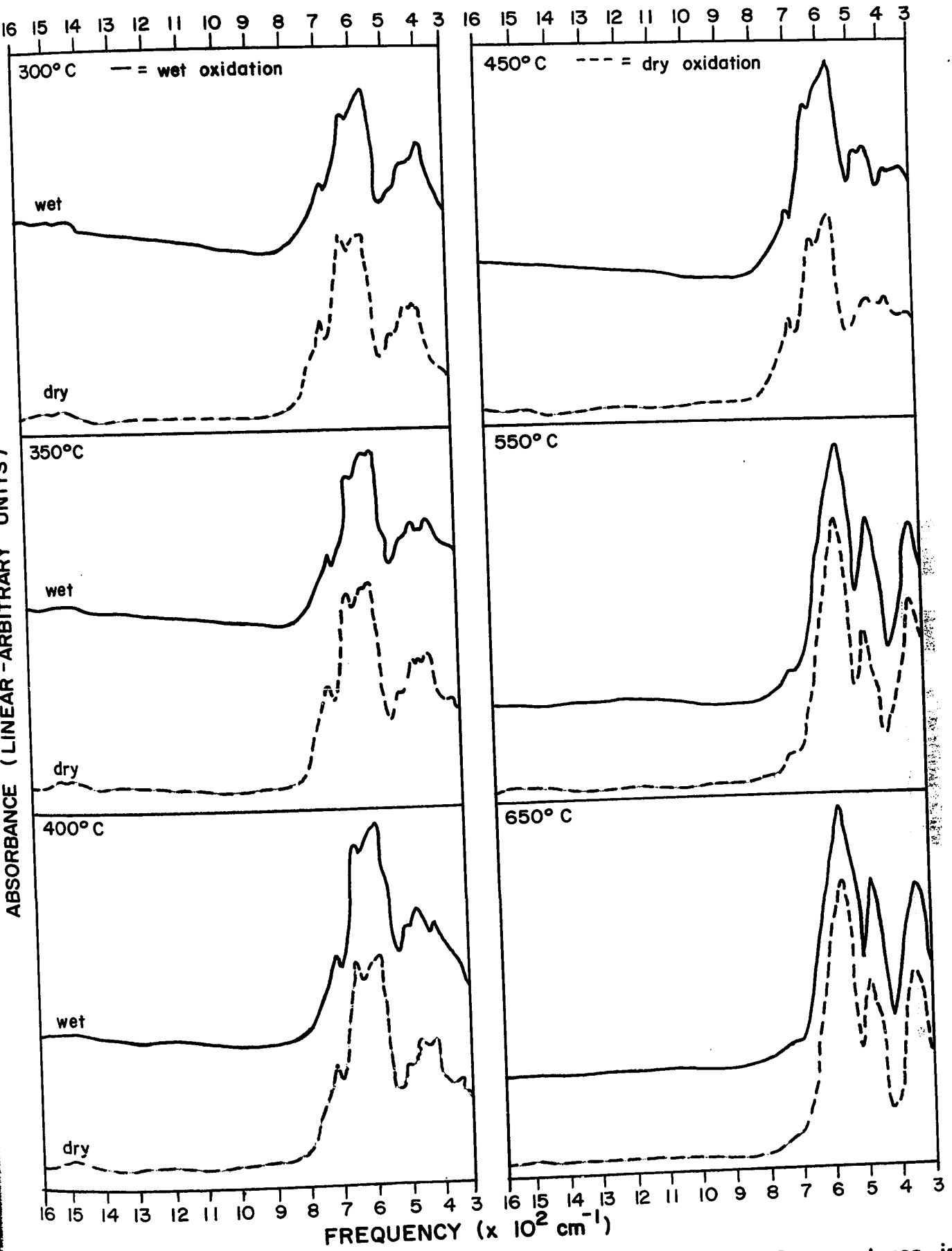

FIGURE 4.4.3 Comparison of Spectral Features at Various Temperatures in the Wet and Dry Oxidation of RMB #5

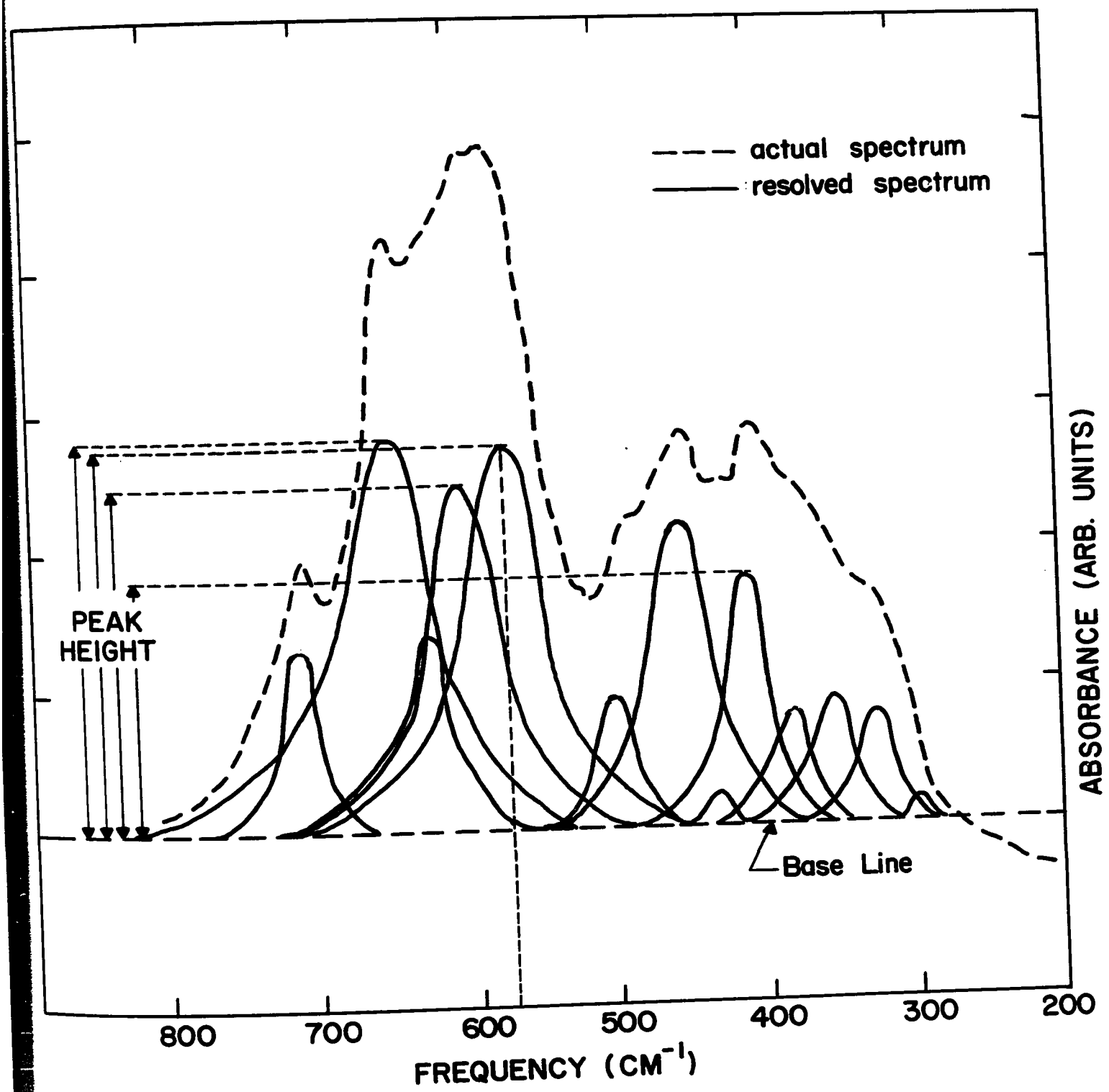

FIGURE 4.4.4 Resolved Spectrum of the 325°C Wet Oxidation Product of RMB #5

TABLE 4.4.3

Computed Bond-Scan Data for Magnetite, Maghemite, and Hematite

Mineral	Lattice Constant (Å)			Octahedral Co-ordination		Tetrahedral Co-ordination	
	Cell-edge a	Ref.	Present Study	Fe-O Bond (Å)	Iron Valence	Fe-O Bond (Å)	Iron Valence
Magnetite (Fe_3O_4)	8.394	42	8.393	2.098	$Fe^{2+} = Fe^{3+}$	1.817	Fe^{3+}
Maghemite (γ-Fe_2O_3)	8.320	43	8.321 - 8.352	2.080	Fe^{3+}	1.801	Fe^{3+}
Hematite (α-Fe_2O_3)	5.035	44	5.029	1.956, 2.084	Fe^{3+}		

TABLE 4.4.4

Infrared Absorption Peak Observations and Assignments for the Products of RMB #5 Oxidized in Dry and Wet Air

Oxidation Product (From Tables 4.4.1 and 4.4.2)	Present Study		Reference Investigations											
			Ref. 31		Ref. 35*		Ref. 36	Ref. 36a	Ref. 36b	Ref. 37*	Ref. 39*	Ref. 40*	Ref. 41	
	Peak (cm^{-1})	Assign	Peak (cm^{-1})	Assign	Peak (cm^{-1})	Assign	Peak (cm^{-1})	Peak (cm^{-1})	Peak (cm^{-1})	Peak (cm^{-1})	Peak (cm^{-1})	Peak (cm^{-1})	Peak (cm^{-1})	Assign
RMB #5 (Magnetite) Fe_3O_4	590(s,b) 400(m,b) 700(sh)	ν_{Fe-O} δ_{O-Fe-O}	570 370-380	$\nu_{Tet\ Fe-O}$ $\nu_{Oct\ Fe-O}$	595 368-397	$\nu_{Tet\ Fe-O}$ $\nu_{Oct\ Fe-O}$	570 360(w)	575(s) 385(s)	570(s,b) 385(m,b)	588-566 (s,b)				
Maghemite (γ-Fe_2O_3)	400(m) 570(s) 590(s) 630(s) 320(w) 420(m) 450(m) 700(w) 1450(v.w.)	ν_{Fe-O} δ_{O-Fe-O}						530(s) 320(s) 451(m)	555 336 468	578(s,b) 448(m,b)				
Hematite (α-Fe_2O_3)	570(s) 480(m) 345(m) 700(w)	ν_{Fe-O} δ_{O-Fe-O}					532 449 391 312	550(s) 470(m) 370(sh) 330(sh)	560(s,b) 468(s) 370(s,b) 325(s)	588-556 476-455 333	1418(w) 980(s) 813(w) 752(m)	571 476 444(sh) 385(sh) 323 235	560(s,b) 452(s,b) 396(w,sp) 383(w,sp) 373(w,sp) 345(m,b) 315(m,b) 287(w,b)	ν_{Fe-O} δ_{O-Fe-O}

Legend

* = wavelength in μ(microns) converted to frequency in wavenumbers (cm^{-1})
ν = stretching vibration, δ = bending or deformation vibration,
Oct = octahedral sublattice, Tet = tetrahedral sublattice, s = strong, m = medium,
w = weak, v.w. = very weak, b = broad, sp = sharp, sh = shoulder

CHAPTER 5

DISCUSSION

5.1 Methods of Preparation

(a) High-Temperature Reduction of α-Fe_2O_3

The reduced preparation proved by XRD analysis, to be pure magnetite, Figure 4.3.1(a). However, subsequent oxidation of the Fe_3O_4 at temperatures between 350 and 1200°C produced no γ-Fe_2O_3 discernible by XRD. The only product of oxidation to 1050°C was a two-phase mixture of α-Fe_2O_3 and Fe_3O_4. The proportion hematite:magnetite increased with rising temperature and above 1050°C, α-Fe_2O_3 existed as a pure phase.

Surface determinations of the Fe_3O_4 and the starting hematite material revealed areas of 0.4 and 11.8 m^2/g, respectively. The Fe_3O_4 surface thus qualitatively confirms Feitknecht's[20] particle-size reaction mechanism relationships. The effect of water content could not be confirmed because of the ready availability of water produced during the reduction by Reaction 1. Comparison of the behaviour of completely anhydrous Fe_3O_4 was therefore impossible.

Figure 4.2.1 illustrates the DT curves of magnetite from reduced hematite produced in atmospheres of flowing argon, wet air, and dry air. Similar studies of natural magnetite have been made by Schmidt and Vermaas[27] while extensive differential thermal investigations of both natural and synthetic magnetite have been made by Mackenzie[28] and Gheith[29].

During wet oxidation, two exotherms appeared at 332 and 358°C, as shown in Figure 4.2.1. The first may be attributed to recrystallization of the magnetite, possibly catalyzed by the adsorbed moisture, while the higher-

temperature exotherm is attributed to the surface oxidation of magnetite, (Fe_3O_4), to hematite, (α-Fe_2O_3), with the creation of a surface layer of hematite surrounding a magnetite core. The recrystallization and surface oxidation processes were confirmed by XRD which revealed the presence of magnetite only at 332°C and magnetite plus hematite at 358°C. Similar conclusions were reached by Gheith[29] in his studies. For dry oxidation, the only peak to appear in this temperature range was that at 327°C, which again was the result of the magnetite-to-hematite surface oxidation. The sharpness of these peaks may be attributed to the uniform particle size of the magnetite. The appearance of the 332°C exotherm during wet oxidation was again possibly due to the catalytic effect of water which enhanced the mobility of the magnetite and thereby promoted recrystallization.

The proposed catalytic effect of water is evidenced by the much greater intensity of the low-temperature exotherms occurring during wet oxidation than those appearing for dry oxidation. Although the magnetite-to-hematite peak occurred at a temperature approximately 30°C higher than for dry oxidation, the combination peak for the 332 and 358°C exotherms covered a broader temperature range and actually commenced at a lower temperature for wet oxidation. This provided further evidence for the catalytic effect of water in the oxidation and recrystallization processes.

The endotherm appearing at 592, 585, and 579°C in argon, dry air, and wet air, respectively, arose from the Curie transition of magnetite from ferrimagnetism to paramagnetism. The endotherms at 685 and 684°C for dry- and wet-air oxidation, respectively, were due to the Neel transition of hematite from antiferromagnetism to paramagnetism.

The relatively small, broad exotherm occurring at 889°C during

wet oxidation resulted from the conversion of magnetite to hematite within the inner core of the crystal grains. The much larger, broader exotherm which appeared at 858°C during dry oxidation resulted from the same oxidation reaction; its intensity was much stronger because a lesser proportion of the particles had previously been converted to hematite at 327°C than was the case for wet oxidation at 358°C. These differences in relative exotherm intensities is again quite likely due to the catalytic effect of water.

(b) Precipitation By Oxidation Of Ammoniacal Ferrous Chloride Solution

Two difficulties in the use of this method were that

(i) the Fe_3O_4 was precipitated from an ammoniacal aqueous solution from which it was impossible to obtain completely anhydrous magnetite by dehydration at moderate temperatures, and

(ii) as with most precipitation methods, the product had a very large specific surface, about 70 m^2/g. The large specific area made the magnetite extremely susceptible to oxidation even while under near-vacuum conditions at room temperature. A discernible colour change from the jet black of magnetite to the reddish brown of maghemite-hematite was noticed after only a few minutes exposure to air at room temperature. In all attempts at precipitation, traces of lepidocrocite (γ-FeO(OH)), goethite, (α-FeO(OH)) and $FeCl_2$ were detected by XRD analysis, inhibiting further investigation of the precipitates. The powder diffraction pattern is shown in Figure 4.3.1(b). All precipitates were of poor crystallinity and produced diffuse diffraction patterns.

(c) Reduction of a Magnetite-Goethite Mixture

As the Mapico Black used for reduction had been prepared by precipitation, it was expected that it would still contain traces of water of

precipitation even after reduction at 400°C. To test this, a thermogravimetric analysis (TGA), Figure 4.2.3, was made on RMB #5 to 800°C in a flowing helium atmosphere. A weight loss of 0.47% occurred over this temperature range and this loss was definitely established as water loss by subsequent vapour chromatographic analysis of the condensed liquid. A marked water loss was observed between 100 and 105°C, after which the loss became barely discernible by TGA. This dehydration effect implies weak hydration of the magnetite and very little, if any, bonding of hydroxyl groups within the magnetite lattice. In other words, the water appears to be physically incorporated rather than bonded chemically.

5.2. XRD Analyses of RMB #1 to RMB #5

XRD analysis of RMB #1 revealed a magnetite pattern with a unit crystal cell edge of 8.393 Å, in close agreement with the accepted value of 8.396 Å[26]. However, four unidentifiable reflections of weak intensity were observed at d = 4.47, 2.33, 1.92, and 1.37 Å. These extra reflections were possibly due to back-reflection. DTA treatment at a temperature increase of 6°C/min in wet and dry air yielded X-ray powder patterns of γ-Fe_2O_3 with traces of α-Fe_2O_3. The specific surface area of RMB #1 was 5.2 m^2/g.

The XRD pattern of RMB #2 was that of single-phase magnetite, but DTA to 330°C and 350°C in wet and dry air, respectively, produced only a two-phase mixture of hematite and magnetite with no trace of maghemite. DTA to 800°C still revealed minor magnetite in hematite. The specific surface of the magnetite was found to be 0.9 m^2/g. According to Feitknecht[20], magnetite of such a specific area oxidizes to hematite only.

RMB #3 consisted of two distinct layers, a black upper phase and a brown lower phase. The low cylinder pressure of CO/CO_2 during the reduction made maintenance of a constant flow of gas very difficult. No attempts at analysis were made.

The XRD pattern of RMB #4 was that of single-phase Fe_3O_4 but with two extra reflections at d = 2.34 and 1.92 Å which again may have resulted from back-reflection. Subsequent DTA and XRD showed a conversion directly from Fe_3O_4 to α-Fe_2O_3 without formation of the metastable intermediate γ-Fe_2O_3. The specific surface area of the Fe_3O_4 was 0.7 m^2/g.

The XRD analysis of RMB #5 showed it to be single-phase magnetite with a cell edge of 8.393 Å. Subsequent DT and XRD analyses indicated its conversion to hematite via the maghemite intermediate. The specific surface of RMB #5 was found to be 6.2 m^2/g.

5.3 DT Analysis of RMB #5

The DTA curves for dry and wet oxidation of RMB #5 are shown in Figure 4.2.2, and the corresponding XRD analyses are listed in Tables 4.4.1 and 4.4.2, respectively. The only peak development was the endotherm at 576°C resulting from the Curie point transition of magnetite from ferrimagnetism to paramagnetism. This transition temperature is in agreement with that found by Mackenzie[28] for synthetic magnetite, the difference in temperature of the endotherm probably being a result of the fine grain size of the magnetite used in the present study and/or the difference in the heating rate used in this study and that of Mackenzie.

In general, the conversion temperatures are much lower than those normally found for magnetite oxidation. The DTA exotherms peaking at 234 and 260°C for the wet and dry oxidations, respectively, result from the $Fe_3O_4 \rightarrow \gamma$-$Fe_2O_3$ conversion, as confirmed by XRD analysis.

Mackenzie[28] found such an exotherm between 275-375°C for synthetic magnetite, while Gheith[29] found a similar exotherm peaking at 210°C in synthetic magnetite oxidized in a hydrous environment. Both authors attribute these temperature differences to variations in particle size and to the catalytic effect of adsorbed water. Mackenzie and Gheith employed heating rates of 10°C/min. and 13.5°C/min., respectively. The 3°C/min. rate used in this study may at least partially account for the higher temperature peaks of Mackenzie and Geith. According to Schröder[30], oxides like γ-Fe_2O_3 may experience under even slight temperature increases, a strong increase in lattice order and a growth in particle size with subsequent loss of water entrapped in lattice flaws or vacancies. The lower temperature of conversion of magnetite to maghemite in the present study confirms the catalytic effect of water, since both the wet and dry oxidations were performed on magnetite of the same grain size. However, the infrared analysis neither confirms nor denies such a catalytic effect, because water was not found by this method. A more complete discussion of the detection of water by infrared absorption analysis will be made later.

Again referring to Figure 4.2.2 and Tables 4.4.1 and 4.4.2, the exotherms peaking at 322 and 345°C in the wet and dry oxidations, respectively, are a result of the conversion of maghemite to hematite. At these temperatures, XRD analysis showed γ-Fe_2O_3, minor α-Fe_2O_3, and a small trace of Fe_3O_4 in the wet product, and γ-Fe_2O_3 and minor α-Fe_2O_3 in the dry product. These may be compared to the temperatures of 590-650 and 460°C as determined by Mackenzie[28] and Gheith[29] for the γ- to α-Fe_2O_3 conversion of synthetic magnetite. These temperature differences are again probably due to effects of grain size and/or water content. For natural magnetite, Gheith found an exotherm between 600 and 1000°C which corresponded to its oxidation directly to hematite.

Two rather broad, flat exotherms were present in the wet oxidation at 285 and 491°C, and in the dry oxidation at 310 and 470°C. These were

probably due to recrystallization processes resulting in energy release and increased stability. In the temperature range of the low-temperature exotherms, the XRD patterns were that of maghemite plus minor magnetite, so

that the exotherm was likely due to recrystallization of the remnant Fe_3O_4 or to the growth of new maghemite. From Tables 4.4.1 and 4.4.2, the XRD patterns for the high-temperature exotherms were that of hematite plus minor maghemite so that the exotherm appears to be due to recrystallization of γ-Fe_2O_3 or to crystal growth of α-Fe_2O_3.

From the XRD analyses it can be seen that the main component of the maghemite-hematite two-phase mixture was hematite at temperatures exceeding 515 and 475°C during dry and wet oxidation, respectively.

5.4. Analysis of Observed Infrared Spectra of RMB #5

From Figure 4.4.1, the absorption peak at 320 cm^{-1} appears as a shoulder at 300°C and as a definite but relatively low-intensity peak from 305 to 450°C in dry air. (The general trend is to gradually increasing intensity with temperature to a maximum at 450°C). For oxidation of RMB #5 by wet air, Figure 4.4.2, the 320-cm^{-1} peak first appears as a slight shoulder at 275°C, and remains a shoulder to 450°C, again with a maximum intensity at 450°C.

The absorption at 345 cm^{-1} first occurs at 515°C during the dry oxidation and at 450°C during wet oxidation. The peak attains a maximum height at 600°C during both dry and wet oxidation.

The 400-cm^{-1} peak occurred in RMB #5 and its oxidation products up to 450°C in dry air and 475°C in wet air, with intensity maxima at 320 and 400°C, respectively. The peak intensities varied little over the temperature ranges in which the maxima were observable.

The same general pattern occurred with the peaks at 420 cm^{-1}. Again the maxima were at 320 and 400°C for the dry and wet oxidations, respectively, but the peaks first appeared at 300 and 275°C, and disappeared

at 450 and 425°C, respectively. The peak resulting from wet oxidation appeared only as a shoulder.

Absorption at 450 cm^{-1} occurred during dry oxidation between 234 and 350°C, with maximum peak height at 320°C. The absorption from wet oxidation occurred between 275 and 450°C with the maximum peak height between 400 and 450°C.

The relative intensities of the absorption at 400, 420, and 450 cm^{-1} varied irregularly following oxidation of RMB #5 with dry air. Figure 4.4.1 shows the appropriate spectra. At 300, 425, and 450°C, the height of the 450-cm^{-1} peak was definitely greater than that of the 400-cm^{-1} absorption but at 305 and 310°C the relative intensities of the two peaks were nearly equal. The 400-cm^{-1} peak definitely predominated in RMB #5 and in its oxidation product at 234°C and between 310 and 400°C. The 420-cm^{-1} peak was generally minor compared to the 400 and 450-cm^{-1} absorptions. Its relative intensity was nearly equal to that of the 400- and 450-cm^{-1} absorptions at 305 and 310°C.

Quite different variations in the three absorptions occurred during wet oxidation. In all cases the 420-cm^{-1} peak occurred as a shoulder of relatively low intensity, whereas the 400-cm^{-1} absorption which predominated at temperatures below 350°C, gradually became relatively less intense, from 375 to 450°C, than the 450-cm^{-1} peak.

The absorption at 480 cm^{-1} was characterized by shouldering from 300 to 450°C, and the appearance of a definite peak from 515 to 760°C for the dry oxidation. Maximum peak intensity occurred at 600°C, although intensities of similar magnitude were observed at 650 and 760 cm^{-1}. For the wet oxidation, Figure 4.4.2, shouldering occurred from 275 to 450°C, and

definite peaking from 475 to 650°C. Maximum intensity was again observed at 600 ± 50°C.

As may be observed in Figures 4.4.1 and 4.4.2, quite dissimilar variations occurred in the relative intensities of the absorption peaks observed at 345 and 480 cm^{-1} resulting from dry and wet oxidation, respectively. For dry oxidation, the 480-cm^{-1} peak was relatively more intense than the 345-cm^{-1} peak at 760 and 515°C, while the 345-cm^{-1} absorption was more intense from 550 to 650°C. For wet oxidation, the 480-cm^{-1} absorption was moderately more intense throughout the temperature range from 475 to 650°C.

For both the dry and wet oxidation products, one of the most intense peaks occurred at 570 cm^{-1}. It was the most intense peak observed at dry oxidation temperatures from 375 to 760°C, and was a major peak to a temperature as low as 300°C. The absorption maximum occurred at 600°C. The 570-cm^{-1} absorption peak from wet oxidation was the predominant peak from 275 to 650°C, and again had maximum intensity at 600°C.

Absorption at 590 cm^{-1} was observed in RMB #5 and the dry oxidation products from 234 to 400°C and in the wet oxidation products from 275 to 450°C. The maxima occurred at 320 and 400°C, respectively. The temperature of the absorption maxima for the 590-cm^{-1} peak was influenced by the strong absorption peak at 570 cm^{-1}. This was particularly true in the case of wet oxidation where the 590-cm^{-1} peak at temperatures from 275 to 325°C and 400 to 425°C appeared as a mere shoulder on the intense 570-cm^{-1} peak.

Infrared absorption at 630 cm^{-1} was observed in the dry oxidation products from 300 to 515°C with maximum peak height occurring at 320°C. The wet oxidation products had similar absorption characteristics at temperatures between 275 and 500°C with the absorption maximum occurring at 400°C.

A comparison of the relative intensities of the absorption peaks at 570, 590, and 630 cm^{-1} for the dry oxidation, Figure 4.4.1 and Table 4.4.1, shows that the 570-cm^{-1} absorption was clearly the most intense at temperatures exceeding 375°C. However, at temperatures between 305 and 320°C, the 630-cm^{-1} peak was the most intense, while at 325°C the 590-cm^{-1} absorption predominated. The intensities of the three peaks were about equal at 300°C. Except at 325°C, the intensity of the 590-cm^{-1} peak was generally weaker than the other two absorptions. The 570-cm^{-1} peak was not observed at temperatures less than 300°C.

For wet oxidation, quite a different situation occurred. In this case, the 570-cm^{-1} absorption first occurred at 275°C. In the temperature range from 275 to 500°C, the relative peak heights were 570 cm^{-1} > 590 cm^{-1} > 630 cm^{-1}. The 590-cm^{-1} absorption was generally only a shoulder over its temperature range of observation, room temperature to 450°C. The 590-cm^{-1} shoulder occurred at temperatures 50°C higher than for dry oxidation.

The similarities and differences between the spectra of the wet and dry oxidation products can best be observed by reference to Figure 4.4.3, in which the spectral region from 300 to 1600 cm^{-1} is shown. The solid-line spectra at the top of the diagrams represent the infrared absorption resulting from wet oxidation, while the hatched-line spectra immediately below represent dry oxidation. Oxidation temperatures of 300, 350, 400, 450, 550, and 650°C were chosen for comparison.

Again referring to Figures and Tables 4.4.1 and 4.4.2, a relatively low-intensity absorption existed at 700 cm^{-1} through the entire temperature range of dry and wet oxidation. Indeed, a weak shoulder was observed at this frequency in RMB #5 itself, so it did not appear to result solely from oxidation. The highest intensity of the peak was observed at 320 and 400°C

in the dry and wet oxidation products, respectively.

The highest-frequency peak observed in the spectra was at 1450 cm^{-1}. It occurred in the temperature ranges from 234 to 450°C and from 275 to 425°C during the dry and wet oxidations, respectively. The peak was broad and weak at all temperatures. In fact, if it had occurred in the absorption region of a strong peak, it would likely have been undetected.

In summary, the spectra of the dry and wet oxidation products were generally very similar. The number and frequencies of absorption peaks were identical in the same temperature ranges of oxidation; ten peaks at low and medium temperatures and four peaks at high temperatures. The 570 cm^{-1} absorption was generally the major peak at all temperatures in both the wet and dry components. At temperatures over 450°C, the 345- and 480-cm^{-1} absorptions were quite intense, though considerably less than the 570-cm^{-1} peak.

Closer examination of the wet and dry spectral analyses permits observation of definite differences between the two resultant spectral groups. During wet oxidation, maximum peak heights were generally attained at equal or greater temperatures than for dry oxidation. Also, the relative variations in peak height between subgroups of spectral peaks, such as those at 400, 420, and 450 cm^{-1}, those at 345 and 480 cm^{-1}, and those at 570, 590, and 630 cm^{-1}, were markedly different in the dry- and wet-oxidation spectra. As earlier stated, these differences are more readily observed by examination of Figure 4.4.3.

5.5. Difficulties Encountered in Assigning Infrared Absorptions

Before proceeding to a fundamental absorption peak assignment of

the observed infrared spectra of RMB #5 and its associated oxidation products, a few of the difficulties encountered in making absorption peak assignments will be outlined.

Difficulties such as chemical changes within the sample and chemical reactions between the sample and the medium have been minimized by careful sample preparation, desiccation of the sample to avoid adsorption and oxidation, and by use of TlBr as the medium to avoid sample-medium reaction. However, crystallographic changes within the sample could have occurred during grinding and/or pelletizing. Such changes would generally tend to produce a more imperfect structure and thereby increase the number of infrared absorption peaks observed.

Waldron[31] was the first investigator to attempt a theoretical, albeit simplified, assignment of observed absorption peaks in ferrites. Waldron considered the rhombohedral primitive unit cell of the ferrite spinels, $M^{II}Fe_2O_4$, to which both magnetite and maghemite belong, every oxygen anion is bonded to 3 octahedral cations, C_O, and 1 tetrahedral cation, C_T. He maintained that the three mutually perpendicular octahedral bonds provide an isotropic force field in which the oxygen is free to oscillate in the three directions in the absence of the tetrahedral bond. The tetrahedral cation C_T then introduces a supplementary restoring force along the C_T-O bond, thereby appearing as a stretching vibration of the tetrahedral group. Thus the highest restoring force is directed along the tetrahedral bond and the stretching vibration of the high-frequency absorption peak must thereby be assigned to this bond.

However, in the case of inverse II-III spinels such as magnetite, such an assignment neglects two important factors: firstly, the effect of strong vibrational interaction between tetrahedral and octahedral subgroups

is ignored; provided that such interactions are of sufficient strength to produce either pseudo-octahedral or pseudo-tetrahedral groups, then the vibrations cannot be assigned to either definite subgroup, but instead are related to complex vibrations of the entire spinel lattice[32]; secondly, even if such interactions are ignored, the proposed assignment will be true only if the C_T-O bond is stronger than the C_O-O bond because the strength of the bond for a given co-ordination number is most strongly dependent on the valency of the cation forming that bond. In the case of magnetite, ferrous ions, Fe^{2+}, occupy only octahedral sites while ferric ions, Fe^{3+}, occupy both octahedral and tetrahedral sites. Therefore, in the case of the inverse spinel on the basis of valency distribution alone, the bond strengths and the consequent vibrational assignments of the octahedral and tetrahedral groups cannot be as clearly defined as in the normal spinel.

In summary, several weaknesses arise from Waldron's[31] description of the bonding. The choice of a primitive rhombohedral cell is much simpler than the full cubic crystallographic cell, and implies a somewhat arbitrary description of the vibrations in terms of tetrahedral and isotropic octahedral force fields. However, octahedral cation sites are occupied equally overall by ferrous and ferric ions, and cannot possibly produce isotropic force fields and distinctive octahedral-type vibrations.

From the foregoing discussion, frequency assignments associated with magnetite and maghemite should not be related to specific co-ordination groups, but to complex vibrations of larger groups such as the entire spinel unit cell. Excellent discussions of the interpretations of spinel vibrations are given in papers by Preudhomme and Tarte[32] and Tarte and Preudhomme[33].

In general, infrared vibrational spectra assignments should not be made on the basis of powder data alone. Most workers feel that oriented single-crystal absorption and reflection data is also necessary in order to make unqualified assignments. However, because of the effect of crystal-size on the magnetite-maghemite conversion, it was not possible in the present study to perform single-crystal investigations. Oriented single crystals minimize the effects of light scattering and lattice distortion outlined earlier.

Before proceeding to a detailed discussion of the infrared spectral assignments of RMB #5 and its oxidation products in dry and wet air, as shown in Figures and Tables 4.4.1 and 4.4.2, respectively, some general observations may be made.

The spectra of both dry- and wet-oxidation products, after heating to approximately 500°C, are rather diffuse and the peaks are assymmetrical. This characteristic is a function of several variables among which are the variation in scatter of the infrared beam by the small range of particle sizes, the numerous orientations of the crystal fragments within the infrared pellet, and the differences in refractive index between the mineral component and the matrix material. The latter is known as the Christiansen effect, and occurs because the refractive index of a material is a function of frequency and has a discontinuity in the frequency region of a strong absorption peak, resulting in a distortion of peak shape if there are many large particles. This is the main reason for grinding of the sample and medium to a finer size than the wavelength region of absorption. However, as discussed earlier, the grinding leads to lattice distortion which, in turn, produces weak peaks that may occur in the frequency region of a fundamental and cause further

distortion of that peak. An excellent discussion of these and similar difficulties associated with infrared absorption analysis of solids has been presented by Phillippi[34].

Referring now to Tables 4.4.1 and 4.4.2 for the dry and wet oxidation of RMB #5, respectively, maghemite exists in solid solution, to varying degrees, with magnetite and/or forms a two-phase mixture with hematite. Under such conditions, it becomes difficult to make definite infrared vibrational assignments since maghemite is not the sole phase present and the other two phases have similar frequency ranges of absorption. However, by careful discrimination of peak height variations and XRD analyses, one can formulate tentative assignments.

5.6. Assignment of Observed Infrared Absorptions

In discussing the infrared absorption spectra of magnetite and its oxidation products, one is confined to considerations of two basic vibrational modes. One is the stretching vibration, ν, of the Fe-O bonds in the mineral lattices, and the other is the bending, or deformation, δ, of the angle between 3 atoms O-Fe-O, or equivalently, Fe-O-Fe, where Fe and O are the "anchor atoms", respectively, around which the bond angle will vary during the vibration. The bond-bending vibrations may be in-plane or out-of-plane of the three atoms involved, and are generally of much less intensity than bond-stretching fundamentals. In fact, the intensity of δ vibrations is approximately equivalent to that of overtone and/or combination peaks.

In reference to Tables and Figures 4.4.1 and 4.4.2, RMB #5 exhibited two broad absorptions at 590 and 400 cm^{-1} which may be assigned to the stretching vibrations of the Fe-O bonds in magnetite. These may be compared

to the peaks found by Waldron[31] at 570 and 370 to 380 cm^{-1} and Hafner[35] at 595 and 368 to 397 cm^{-1}, and assigned to the tetrahedral and octahedral sublattices, respectively. Liese[36], Estep et al.[36a], and McDevitt and Baun[36b] observed two peaks at 570 ± 5 cm^{-1} and 360 cm^{-1}, 575 and 385 cm^{-1}, and 570 and 385 cm^{-1}, respectively, while Maekawa and Terada[37] observed one peak only at 566 to 588 cm^{-1} in synthetic magnetite. Of the foregoing peaks, only those of Liese[36] and Estep et al.[36a] were observed in natural magnetite. A variation of 30 to 40 cm^{-1} occurred between the peak frequencies of individual samples. This variation may have been due to differences in preparative procedures or variations in lattice parameters or impurities.

The shoulder existing at 700 cm^{-1} was probably due to a δ vibration.

One can observe from the spectra in Tables 4.4.1 and 4.4.2 that the vibrational peaks of RMB #5 are much broader and more poorly defined than those of its oxidation products. In fact, they are Gaussian rather than Lorentzian in nature. This effect may arise from two factors: the relatively poor crystallinity of the magnetite compared to its oxidation products; and that magnetite contains both ferrous and ferric ions in octahedral sites and ferric ions in tetrahedral sites so that, if one assumes lattice vibrations predominating over specific co-ordination vibrations, the net vibrational effect is one of superimposing the Fe-O stretching vibrations for both types of sites and ions. The same reasoning will hold for the bending vibrations δ which are probably superimposed at some frequency within the two main absorption peaks.

XRD analysis of RMB #5 confirmed the existence of pure magnetite with a unit cell edge of 8.393 Å.

In the temperature ranges of 300 to 450°C and 275 to 450°C, for the dry and wet oxidation products, respectively, ten infrared absorption peaks were observed at 320, 400, 420, 450, 480, 570, 590, 630, 700, and 1450 cm^{-1}.

Of these, the peaks at 400, 570, 590, and 630 cm^{-1} were the most intense and will be assumed due to the stretching vibrations ν of the Fe-O bonds. The assignment of the 400- and 590-cm^{-1} peaks to the Fe-O stretch is consistent with their assignment for pure magnetite, since in this temperature range the peaks were intense and a major component was found by XRD analysis to be maghemite which has an inverse spinel crystal structure like magnetite. Based solely on intensity considerations, the 570 and 630 cm^{-1} absorptions should also be those of $^{\nu}$Fe-O.

The relatively weak peaks at 320, 420, 450, 700, and 1450 cm^{-1} are assumed to be due to the bending vibrations δ of the O-Fe-O bonds. The differentiation between stretching and bending vibrations is rather difficult because of the interspersion, particularly of hematite peaks, amongst the other spectral features within these temperature ranges, resulting in shouldering. Some of the frequencies could be due to the stretching vibrations of the maghemite lattice because of the lower symmetry resulting from ordered vacancies. Absorption at 480 cm^{-1} was likely due to a stretching vibration in hematite.

The only previously reported infrared vibrational investigations of maghemite in the spectral region of this study were recorded by Maekawa and Terada[37], Estep *et al.*[36a], and McDevitt and Baun[36b], who reported absorptions at 448 and 578 cm^{-1}, 320, 451, and 530 cm^{-1}, 336, 468, and 555 cm^{-1}, respectively, which they did not attempt to assign.

From the XRD analyses listed in Tables 4.4.1 and 4.4.2, it can be seen that the main component of the maghemite-hematite two-phase mixture was hematite at temperatures exceeding 515 and 475°C during dry and wet oxidation, respectively.

At these and higher temperatures the infrared spectra were characterized by three relatively intense absorptions at 345, 480, and 570 cm^{-1}.

Of these, the 570-cm^{-1} peak may definitely be assigned to the ν_{Fe-O} mode, because it had the greatest intensity.

However, some doubt exists regarding the assignment of the peaks at 345 and 480 cm^{-1}. Since the hexagonal unit cell of hematite contains two distinctly different Fe-O bond distances of 1.941 and 2.119 Å[38], one should therefore, expect to observe at least two distinct Fe-O stretching frequencies related to these bonds, and either or both of the 345 and 480 cm^{-1} peaks may be due to ν_{Fe-O}. Both are of sufficient strength to be a result of stretching vibrations.

The weak peak appearing at 700 cm^{-1} was observed only as a slight shoulder and as a result of its low intensity may be assigned to the deformation vibration δ_{O-Fe-O}.

Again referring to Figure 4.2.2 and Tables 4.4.1 and 4.4.2, hematite was initially formed at 322 and 345°C in wet and dry air, respectively. As the temperature was increased, a greater proportion of the maghemite-hematite two-phase mixture was converted to hematite, until at temperatures of 475 and 515°C, XRD analysis revealed mainly hematite. At a temperature of 650°C, XRD analysis showed hematite only, and the length of the unit cell edge a of the dry oxidation product was 5.029 Å, in good agreement with that of 5.035 Å found by Blake *et al.*[38] for synthetic hematite. As the temperature was increased to 475 and 515°C for wet and dry oxidation, respectively, the infrared spectra revealed disappearance of the absorption peaks assigned to maghemite and a corresponding preponderance of the absorptions assigned to hematite. This was in very good agreement with the findings of DT and XRD analyses; indeed, agreement was excellent throughout the entire temperature range of study.

Several infrared investigations have been made on both natural and synthetic hematite in the spectral region of the present study. Natural α-Fe_2O_3 from England, Minnesota, Minnesota, and from an unknown origin have been analysed by infrared absorption by Liese[36], Estep et al.[36a], Hunt et al.[39], and Mitsuishi et al.[40], respectively. Liese[36] found absorptions at 532, 449, 391, and 312 cm^{-1}, Estep et al. at 550, 470, 370, and 330 cm^{-1}, Hunt et al.[39] at 1418, 980, 813, and 752 cm^{-1}, and Mitsuishi et al.[40] at 571, 476, 444, 385, 323, and 235 cm^{-1}. None of these workers attempted to assign the observed peaks. Again, the wide variance in spectral regions of absorption was likely a result of impurities, matrix interference, or inadequate grinding.

Rao and Rao[41] have examined synthetic hematite by infrared absorption. They observed absorptions at 560 and 452 cm^{-1}, which they assigned to ν_{Fe-O}, and less intense peaks at 396, 383, 373, 345, 315, and 287 cm^{-1} which they tentatively assigned to δ_{O-Fe-O}. McDevitt and Baun[36b] observed absorptions at 560, 468, 370 and 325 cm^{-1} in commercial hematite in which maghemite was a suspected impurity.

Because the absorption frequencies of the Fe-O bonds are directly associated with the bond lengths, bond-scan analyses were made of magnetite, maghemite and hematite. The lattice constants and atomic co-ordinates so employed were those of Tombs and Rooksby[42] for magnetite, Ueda and Hasegawa[43] for maghemite, and Wyckoff[44] for hematite. The computed bond-lengths and associated valence and co-ordination groups are listed in Table 4.4.3.

In summary, the observed absorption peaks and their assignments are enumerated in Table 4.4.4. Also listed in Table 4.4.4 are the spectral observations of both natural and synthetic samples of magnetite, maghemite, and hematite and their proposed assignments as postulated by other workers.

From the bond-length data of the foregoing Table, one can assume that the 590-cm^{-1} absorption common to both magnetite and maghemite results

from the stretching vibration of the respective 1.817 and 1.801Å bonds. The absorption at 570 cm^{-1} in hematite is likely due to the vibration of the 1.956Å bond.

On the basis of bond-length considerations alone, one may conclude that the 400-cm^{-1} absorption in magnetite and maghemite results from stretching of the 2.098 and 2.080Å bonds, respectively. Likewise, stretching of the 2.084Å bond probably results from absorption at either 345 or 480 cm^{-1} in hematite.

The spectral absorption patterns of magnetite and hematite were relatively simple, with only three and four respective absorption peaks observed. However, in the mid-temperature region of oxidation, from roughly 300 to 450°C, the spectra became quite complex as a result of admixture in various proportions of at least two of the three phases: magnetite, maghemite, and hematite. At no temperature was there clear evidence of water absorption nor undeniable evidence, based on infrared analyses alone, for the catalytic effect of water in the conversion processes. In general, the spectral features of the wet and dry oxidation products were very similar save for the relative intensities of certain aforementioned absorption peaks.

The only real discrepancy between the XRD, DT, and infrared methods of analysis was in regard to water. The DTA indicated evidence of the catalytic effect of water in the magnetite-to-maghemite conversion, but no trace of water was determined by infrared analysis. A possible explanation of these apparently conflicting data will be presented in the following section.

5.7. Infrared Determination of Water

From Figure 4.2.2 the endotherm between 110 and 200°C associated with the release of adsorbed water was absent in the present investigation as

a result of pre-drying the RMB #5 at 105°C before the oxidation analyses. The water associated with the conversion dynamics of the wet oxidation should therefore have been provided only by the water-vapour saturated air during the process, although residual adsorbed water was likely present during both the wet and dry analyses.

It is clear from the theoretical discussion, subsection 2.4.6, of the infrared absorption features of water and its associated hydroxo groupings that there was negligible water or OH content in the oxidation products under examination. The lack of absorption features from 3600 to 3200 cm^{-1} due to OH stretches, and the similar lack of structure from 1630 to 1600 cm^{-1}, characteristic of HOH bending vibrations, precludes the possibility of the presence of either water or hydroxo groupings. However, the low-temperature DTA exotherm at 322°C, Figure 4.2.2, in the wet air oxidation indicates at least a catalytic effect, if not actual adsorption or bonding, resulting from the presence of water. If such a catalytic effect occurs, it must do so either via a short-lived intermediate structure or by a transport mechanism in which water carries oxygen atoms to the reaction sites in the magnetite but does not itself associate with the magnetite lattice.

A possible reaction mechanism for the intermediate type of structure would be:

$$2\left[Fe^{2+}(Fe_2O_4)^{=}\right] + H_2O + \tfrac{1}{2}O_2$$

$$\rightarrow 2\left[Fe^{3+}(OH)^{-}(Fe_2O_4)^{=}\right] \rightarrow 3\gamma\text{-}Fe_2O_3 + H_2O \quad (A)$$

in which the intermediate is represented by the square bracket. It must rapidly dissociate to maghemite because a moderately long-lived intermediate would exhibit the normal hydroxo vibrations upon infrared analysis. The hydroxyl ions in the intermediate would fill the vacancies in the octahedral

and tetrahedral interstices of the magnetite lattice. Such a proposed intermediate is in agreement with the proposals of David and Welch[5] and Sinha and Sinha[6] regarding the filling of cation vacancies by OH^- ions with the simultaneous oxidation of ferrous iron to the ferric state.

Such a process would likely be a surface phenomenon because the intermediate is apparently short-lived. This would result in the formation of a mixed phase consisting of surface-oxidized magnetite (maghemite) and unoxidized magnetite. Such a mixed phase occurs during wet oxidation at temperatures of 275 and 300°, Table 4.4.2, and during dry oxidation at temperatures of 234 and 300°C, Table 4.4.1. However, as stated earlier, residual water was likely present during the dry oxidation, although it was not detected by either DTA or infrared observations, and this was possibly sufficient to act as an intermediate component for the magnetite-to-maghemite conversion, even though no direct evidence existed for the necessity of water in the conversion process.

5.8. An Unsuccessful Attempt to Estimate Activation Energies

An attempt was made to evaluate the activation energies by the use of Equations 2.4.5(c) and 2.4.5(e) for first- and second-order reactions, respectively. The resolved peak heights of the assigned absorptions were assumed directly proportional to the initial and final reactant concentrations c_1 and c_2, respectively, and the peak heights and their corresponding temperatures were then incorporated in both of the above equations.

However, such an assumption regarding the direct proportionality of the peak heights to the concentrations would be true only if the reactant under observation was the only one present to vibrate at that specific frequency.

In the present study, such was not the case. Rather, the 400 and 590-cm^{-1} peaks which have been assigned to the fundamental stretching frequencies, ν, of magnetite, are likewise present as fundamentals in maghemite, the oxidation product. Likewise, the 570-cm^{-1} absorption in maghemite also absorbs strongly in hematite. Therefore, in order to employ the resolved absorption peak-heights or intensities as reactant concentration parameters, the portion due to the reaction products must be deducted from the total peak intensity. This cannot be done because the extinction coefficients for the minerals are unknown.

Possibly the best choice of frequencies for the activation energy calculation for the maghemite-to-hematite reaction was 630 cm^{-1}. This peak was relatively intense within the maghemite temperature region and was observed only with the presence of maghemite. However, this frequency was in close proximity to, and in fact appeared as a shoulder on, the broad, intense 570 and 590-cm^{-1} peaks, and resolution of the peaks was at best approximate. Further difficulties arose because of the overlapping temperature ranges of stability of the minerals; the simultaneous production of maghemite and enhancement of the 630-cm^{-1} peak was counteracted by the diminution of the 630-cm^{-1} peak because of the production of hematite which does not absorb in this spectral region. At no temperature was maghemite the sole phase present so that such interference was probable at all frequencies of absorption.

A major weakness in the computation of activation energies by the preceding method is in the assumption of pure first- and second-order reactions. Instead, probably several reactions are occurring simultaneously. Under the conditions used, competing processes are likely consecutive and/or simultaneous reactions:

Consecutive: $2Fe_3O_4 + \frac{1}{2}O_2 \xrightarrow{k_1} 3\gamma\text{-}Fe_2O_3 \xrightarrow{k_2} 3\alpha\text{-}Fe_2O_3$

Simultaneous: $2Fe_3O_4 + \frac{1}{2}O_2 \xrightarrow{k_3} 3\gamma\text{-}Fe_2O_3$

$2Fe_3O_4 + \frac{1}{2}O_2 \xrightarrow{k_4} 3\alpha\text{-}Fe_2O_3$

The occurrence of these competing processes is evidenced by the occurrence of the three minerals in widely overlapping temperature ranges.

Parameters such as the rate of diffusion of iron ions into the magnetite lattice through surface product layers and the possible, but not proven, catalytic effect of water, should be included in the complete expression of the reaction kinetics. No direct quantitative evidence for such effects was possible in this investigation.

Other problems in the computation of activation energies were physical in nature. Although the infrared pellets for analysis were very carefully prepared with regard to mineral concentration, the author had great difficulty in obtaining a completely uniform matrix-mineral mixture, so that, in some pellets, opaque aggregations of mineral occurred, to cause increased infrared absorption.

Considerable difficulty was experienced in resolving the spectra with the Dupont Peak Resolver 310. Theoretically, each change of slope occurring on the shoulders or sides of a peak should be resolved into individual components whose sum equals the unresolved peak. However, in this investigation, the peaks were closely grouped with, at times, considerable shouldering, so that it became impossible to resolve the spectra completely. This was particularly true in the middle temperature range of analysis, where hematite co-existed as a separate phase with magnetite and maghemite.

In summary, the conversion reactions magnetite → maghemite → hematite do not appear to occur by simple pure first- or second-order processes, but likely involve side reactions and possibly intermediate formation with water to form a hydroxo complex.

CHAPTER 6

CONCLUSIONS

From the foregoing discussion, the following conclusions can be drawn:

1. The temperature of conversion of synthetic magnetite to maghemite and hematite appears to be strongly dependent on the magnetite particle size and the presence of water. Maghemite will form if the specific surface of synthetic magnetite is 5.2 m^2/g but not if it is 0.9 m^2/g.
2. Maghemite did not appear to form a single phase by itself but was always found in combination with either magnetite or hematite or both. It seems to occur as a surface layer by-product of oxidation.
3. Oxidation of magnetite to maghemite and conversion of maghemite to hematite occurs at a temperature about 25°C lower in a wet atmosphere than in an anhydrous atmosphere. An hydroxo intermediate may be postulated to explain the reduced temperature of formation of maghemite and its subsequent conversion to hematite.
4. No trace of water or hydroxide was found by infrared analyses of the mixed maghemite phases, so the proposed hydroxo complex could be a short-lived intermediate.
5. An attempt was made to assign the observed infrared absorption vibrations of magnetite, maghemite, and hematite to either the stretching or bending modes. Magnetite appeared to have two stretching and one bending mode; maghemite, four stretching and five bending modes; and hematite, three stretching and one bending mode.
6. It was not possible to determine the activation energies for the magnetite-maghemite and maghemite-hematite reactions using fundamental absorption

peak intensities because the respective extinction coefficients are not known and because of spectral interference. It appears that the reactions are complex in nature and are neither pure first- nor pure second-order reactions; this supports the supposition of either hydroxo intermediate formation or the occurrence of simultaneous reactions.

CHAPTER 7

SUGGESTIONS FOR FURTHER WORK

More direct evidence is required concerning the catalytic effect of water on the oxidation of magnetite. If the short-lived hydroxo intermediate proposed in Subsection 5.7 occurs, the only means of definitely establishing its existence by infrared analysis would be by the *in situ* oxidation of magnetite in a moist atmosphere at changing temperature. Such an *in situ* investigation would also facilitate the determination of the activation energies and related thermochemical properties since a very thin layer of magnetite could be suspended between transparent windows during the oxidation, thus minimizing sources of error such as inhomogeneity due to insufficient matrix-mineral mixing and crystal imperfections due to grinding and/or pelletizing. Heating chambers for such a study have been developed, but as yet no suitable window-material has been found which is transparent over the spectral region of interest.

Single-crystal absorption and/or reflection data is necessary for unqualified spectral peak assignments. Large pure single crystals of magnetite have been grown by Smiltens[45], but they have not been studied by infrared. Due to the apparent particle-size dependence of maghemite production, it is unlikely that crystals of sufficient size for such a study can be grown.

Theoretically, any analytical method which is adaptable to an *in situ* investigation of magnetite could be used to determine the activation energies for the reactions. Two such procedures could be Moessbauer spectroscopy, concerning magnetic properties, and XRD analysis, concerning atomic structural properties. The chief difficulty would be in developing suitable heating chambers for such studies. The principal advantage of Moessbauer investigations would be their freedom from spectral interference by neighbouring peaks.

REFERENCES

1. Hägg, G., Zeits. Krist., 1935, B29, 95.
2. Verwey, E.J.W., Zeits. Krist., 1935, 91, 65.
3. Braun, P.B., Nature, 1952, 170, 1123.
4. Aharoni, A., E.H. Frei and M. Schieber, J. Phys. Chem. Solids, 1962, 23, 545.
5. David, I. and A.J.E. Welch, Trans. Faraday Soc., 1956, 52, 1642.
6. Sinha, K.P. and A.P.B. Sinha, Zeits. Anorg. Allgem. Chem., 1957, 293, 228.

6a. Bagin, V.I. and R.S. Rybak, Phys. Solid Earth, 1970, 6, 395.

6b. van Rensburg, W.C.J., Ann. Geol. Opname, Repub. A.-Afr., 1966, 5, 93.

6c. Schwertmann, U., Fortschr. Mineral., 1968, 46, 274.

6d. Daniels, J.M. and A. Rosencwaig, J. Phys. Chem. Solids, 1969, 30, 1561.

6e. Takada, T., M. Kiyama, Y. Bando, and T. Shinjo, Bull. Inst. Chem. Res., Kyoto Univ., 1969, 47, 298.

6f. Palache, C., H. Berman, and C. Frondel, Dana's System of Mineralogy, 7th Ed., Vol. I, 1944, John Wiley and Sons, N.Y.

7. Robbins, J., Chem. News, 1859, 1, 11.
8. Wagner, P.A., Econ. Geol., 1927, 22, 845.
9. Sosman, R.B. and E. Posnjak, J. Wash. Acad. Sci., 1925, 15, 329.
10. Twenhofel, L.H., Econ. Geol., 1927, 22, 180.

10a. McLeod, C.R., Geol. Survey Can., 1970, Paper 70-7,1.

11. Love, C.H. and J.W. Ayers, Protective and Decorative Coatings, Vol. II, 1942, J.J. Mattiello, John Wiley and Sons, N.Y.
12. Gorter, E.W.,Philips Research Reports, 1954, 9, 295.

12a. Claassen, A.A., Proc. Phys. Soc. (London), 1926, 38, 482.

13. Haul, R. and T. Schoon, Zeits. Phys. Chem., 1939, 44B, 216.

14. Hasegawa, K., N. Wada, T. Ichinokawa and R. Ueda, Sci. and Eng. Bull. 1959, #12, 15. XRD pattern from ASTM Card #15-615.

15. Ferguson, G.A. and M. Hass, Phys. Rev. 1958, 112, 1130.

15a. van Oosterhout, G.W., and C.J.M. Rooijmans, Nature, 1958, 181, 44.

16. Pauling, L. and S.B. Hendricks, J. Am. Chem. Soc., 1925, 47, 781. XRD pattern from Berry, L.G. and R.M. Thompson, "X-Ray Powder Data for Ore Minerals: The Peacock Atlas", Geol. Soc. Am. Mem., 1962, No. 85, 174.

17. Blake, R.L., R.E. Hessevick, T. Zoltai and L.W. Finger, Am. Mineral., 1966, 51, 123.

18. Ferraro, J.R., R. Driver, W.R. Walker and W. Wozniak, Inorg. Chem., 1967, 6, 1586.

19. Mackay, A.L., Proc. Int. Symp. React. Solids, 4th, 1961, Elsevier, Amsterdam, p. 571.

20. Feitknecht, W., Pure Appl. Chem., 1964, 9, 423.

21. Feitknecht, W. and H.W. Lehmann, Helv. Chim. Acta, 1959, 42, 2035.

22. LeFort, J., Compt. rend., 1869, 69, 179.

23. Eichenberger, W., Licentiate Thesis, 1958, Bern, Switzerland.

24. Donaldson, E.M., Anal. Chem., 1969, 41, 501.

25. Gabe, E.J., unpublished data.

26. Basta, E.Z., Min. Mag., 1957, 31, 431. XRD pattern from ASTM Card #11-614.

27. Schmidt, E.R. and F.H.S. Vermaas, Am. Mineral., 1955, 40, 422.

28. Mackenzie, R.C., "The Differential Thermal Investigation of Clays", Min. Soc., London, 1957, Ch. XII, 299.

29. Gheith, M.A., Am. J. Sci., 1952, 250, 677.

30. Schröder, W., Zeits. Elekt., 1940, 46, 680.

31. Waldron, R.D., Phys. Rev., 1955, 99, 1727.

32. Preudhomme, J. and P. Tarte, Spec. Acta, 1971, 27A, 961.

33. Tarte, P. and J. Preudhomme, Acta Cryst., 1963, 16, 227.

34. Phillippi, C.M., Air Force Materials Lab. Tech. Rep., 1968, AFML-TR-68-317.

35. Hafner, S., Zeits. Krist., 1961, 115, 331.

36. Liese, H.C., Am. Mineral., 1967, 52, 1198.

36a. Estep, P.A., J.A. Kovach, C. Karr, E.E. Childers, and A.L. Hiser, Am. Chem. Soc., Div. Fuel Chem., Prepr., 1969, 13, 18.

36b. McDevitt, N.T. and W.L. Baun, Spec. Acta, 1964, 20, 799.

37. Maekawa, T. and M. Terada, J. Jap. Inst. Metals, 1965, 29, 421.

38. Blake, R.L., T. Zoltai, R.E. Hessevick, and L.W. Finger, U.S. Bur. Mines, Repts. Invest. 7384, 1970, 1.

39. Hunt, J.M., M.P. Wisherd and L.C. Bonham, Anal. Chem., 1950, 22, 1478.

40. Mitsuishi, A., H. Yoshinaga, S. Fujita and Y. Suemoto, Jap. J. Appl. Phys., 1962, 1, 1.

41. Rao, G.V.S., C.N.R. Rao and J.R. Ferraro, Appl. Spect., 1970, 24, 436.

42. Tombs, N.C. and H.P. Rooksby, Acta Cryst., 1951, 4, 474.

43. Ueda, R. and K. Hasegawa, J. Phys. Soc. Jap., 1962, 17, 391.

44. Wyckoff, R.W.G., "Crystal Structures", John Wiley and Sons, New York, 2nd Ed., 1964, Vol. 2, 7.

45. Smiltens, J., J. Chem. Phys., 1952, 20, 990.